J. Inst. Eng. India Ser. A (December 2025) 106(4):1147–1178
https://doi.org/10.1007/s40030-025-00921-w

ORIGINAL CONTRIBUTION

Analysis of Century Old Masonry Tower of Indo-Sarascenic style: Visual Inspection, NDT and FEM

Ambareesh Kumar[1] · Kumar Pallav[2]

Received: 28 February 2025 / Accepted: 17 August 2025 / Published online: 5 September 2025

Abstract This study investigates assessing the structural behaviour and efficacy of historical masonry towers constructed using unreinforced masonry techniques. Four such towers were subjected to numerical analysis through the finite element method (FEM) in the aftermath of the 2015 Nepal earthquake. The initial stages involved visual inspections to gauge the towers' structural conditions. Using these visual assessments and data from existing records, precise geometrical plans and elevations for each tower were incorporated into AutoCAD. Subsequently, comprehensive 3D-models of the towers were subjected to complex analysis containing static and dynamic assessments. Employing the ANSYS Workbench tool (version-14) with Indian codal provisions and guidelines (IS:875, Part I-III) offered a distinct insight into the study. Material properties of the towers are accomplished through non-destructive testing (NDT), incorporating Rebound Hammer and Ultrasonic Pulse velocity methods. Site visual inspections unveiled significant damage to integral tower components such as arches, openings, and masonry walls. This observation highlights susceptibility to abrupt structural elements and material failures. Furthermore, utilising NDT data as a computational input stimulated insights into the substantial influence of tower geometry—encircling factors like slenderness, wall thickness, and openings-on structural capacity regarding stresses, deformations, and overall performance. The research highlighting vulnerabilities and structural complexities extends to suggesting mitigation strategies, notably retrofitting, that can preserve these valuable remains of history.

Keywords Tower · Unreinforced masonry · Visual inspection · Cracks and damages · Non-destructive testing · Geometrical drawings and Finite element modelling · Static and dynamic analysis

✉ Ambareesh Kumar
ambar006@gmail.com

Kumar Pallav
kumarp@cput.ac.za

1 Civil Engineering Department, Motilal Nehru National Institute of Technology Allahabad, Prayagraj, Uttar Pradesh 211004, India

2 Department of Civil Engineering and Surveying, Cape Peninsula University of Technology, Bellville, Cape Town 7530, South Africa

Introduction

Masonry construction, an ancient building technique, persists in rural areas of underdeveloped nations. Over 70 percent of global structures are masonry-based [1], found both as stand-alone buildings and integrated parts of urban landscapes, such as churches, castles, and city walls. In this study, the towers are constructed independently within the university premises. Protecting historical monuments from structural risks is a complex study. It involves analyzing their current state, investigating their historical context and construction techniques, identifying present damage causes, and designing rehabilitation and prevention strategies. While India's historic structures, such as the Taj Mahal, Qutub Minar, and Rang Ghar, have received some attention [2–4], numerous studies focus on in-situ surveys, damage assessment, and seismic evaluations [5–8].

Seismic response analysis, particularly post-failure, has been conducted for masonry towers [9–11]. We develop three-dimensional (3D) Finite Element (FE) models for each tower, performing static and dynamic analyses (modal approach). Unreinforced masonry structures' behaviour and damage patterns have been investigated through various numerical models, including finite element and discrete element approaches [12–14]. When unreliable connections exist, as seen in these towers, smaller portions susceptible to local collapse mechanisms are analyzed in 3D. While prior literature has discussed masonry's mechanical behaviour in the context of FE modelling [15, 16], there's a lack of in-depth exploration of its nonlinear phase characterized by crack propagation.

Assessing the structural vulnerability of historic buildings requires considering both normal loads (weight, snow, wind, etc.) and exceptional events (earthquakes, temperature, atmospheric effects, etc.) [8, 17–19]. This research contributes to understanding masonry structures' response to seismic events, aiding in their preservation and resilience against routine and exceptional loads.

The comprehensive study encompassed historical and archaeological investigations [20], analyses of the historical structures [11, 21, 22], non-destructive testing of masonry [15], examination and evaluation of wooden components, windows, and doors. Inadequate maintenance, particularly on roofs, led to water infiltration into wooden elements and vertical walls. Non-destructive testing and numerical assessments were conducted on the roofs and main vertical walls to determine their structural vulnerabilities and the extent of the damage. [23] uses a magnetically charged system search and particle swarm optimization for damage detection. Seismic analyses of masonry towers involved experimental analyses such as destructive, minor destructive, and non-destructive testing to assess mechanical properties [15, 16, 24, 25].

Accurate assessment of these structures against various forces, including static (gravity, live loads) and dynamic (modal, time history), holds significant importance for historical, social, and artistic reasons. Dynamic identification analyses have been widely employed to evaluate the performance of various structural elements, including towers, arches, vaults, walls, domes, and façades [26–29]. The dynamic analyses were performed on detailed 3D-FE models of the towers, utilizing seismic, Elasto-Plastic time history, and vulnerability analysis methods [11, 30, 31]. [32] shows the optimal analysis of structures by utilizing their symmetry and regularity. Previous research has revealed the high response of ancient masonry towers under horizontal loads. The numerical outcomes were juxtaposed with stress and deformation responses obtained through static and dynamic analysis procedures. Results from static procedures demonstrated good agreement with those from time-consuming non-linear dynamic simulations, with a slightly less conservative trend.

Past seismic events have been the focus of damage and failure analyses [11, 21, 22, 30, 33–38], leading to post-earthquake investigations. These investigations encompassed direct surveys, historical and documentary research, material testing, and ambient vibration tests [39, 40] to identify critical locations within structures for improvement. Specific research focused on in-depth studies of the collapsed and damaged mechanisms of worldwide unreinforced masonry structures [41–44]. Building upon these studies, innovative methods and techniques for strengthening, retrofitting, rehabilitating, and preserving traditional materials (mortar and bricks) were discussed, along with strategies for structural upgrading [1, 10, 45, 46].

Applying predictive models and modern construction assessments can mislead in gauging structural safety and result in unnecessary or detrimental interventions. Moreover, uncertainties in material properties and their nonlinear behaviour, coupled with potential ineffective connections among diverse structural elements (wood, stone, mortar, iron), make analyzing the overall structural response to generic loads exceedingly complex [42, 47–52].

This study focuses on a quartet of towers within the building at Allahabad University, as depicted in Fig. 1. These towers exhibit distinct variations in their locations, geometrical designs, and dimensions, each serving diverse purposes. A comprehensive investigation has honed in on a pivotal tower element in light of these variations. The objective is to acquire in-depth insights into the structural landscape encompassing attributes like wall thickness, geometric configurations, materials, and heights. Additionally, the study explores construction techniques, including geometric styles, structural elements, and materials. Aspects of cracks, damage patterns, failures, and collapses, extending to plaster, binding materials, structural components, and decorative elements, also fall within the scope of the examination.

Visual inspections have yielded valuable data regarding geometric cross-sectional intricacies and material composition. Geometric cross-sectional drawings and 3D-FE models were subsequently created through visual assessments using AutoCAD and ANSYS-Workbench [53]. These detailed geometric renderings maintained real-world dimensions, while macro-modelling techniques were employed to prepare FE models. Post-visual inspection, geometric modelling, and non-destructive testing were conducted across all tower components, encompassing walls and stones. Rebound Hammer (RH) and Ultrasonic Pulse Velocity (UPV) tests were conducted at corresponding locations on accessible floor levels to approximate the mechanical properties of brick masonry and stone materials. Before testing, thorough assessments were carried out to ensure the absence of moisture, cracks, deterioration, and related factors to guarantee the accuracy. Static and dynamic responses were then derived based on the experimental mechanical properties of the towers after the Nepal earthquake in 2015. Adhering to IS code provisions and guidelines, stress and deformation capacities were evaluated through static analyses (considering own weight and live load) and dynamic analyses (comprising modal and

Fig. 1 Structural view of the unreinforced masonry Senate Hall building with towers

time history analysis) using ground motion response data specific to Allahabad city (Now Prayagraj city).

About Prayagraj (previously Allahabad City) and the Senate Hall (SH) Building

Located at 25°28′N latitude and 81°54′E longitude, with an elevation of 98 m above sea level, situated at the confluence of the Ganges and Yamuna rivers, the city was originally named Prayag, signifying the "place of offerings" due to the confluence known as Sangam. The name was later changed by Mughal Emperor Akbar in 1583. As of 2011, Allahabad ranks as the seventh most populous city in Uttar Pradesh and the thirty-sixth most populous in India, with around 1.11 million residents and 1.21 million in its metropolitan region. In 2011, it held 130th among the world's fastest-growing cities [20]. Renowned for the Kumbha Mela, a massive gathering during the Magh month (January and February), the city boasts various historic structures from different eras, including the Allahabad Fort (1583), Khusro Bagh (1622), Ulta Qila (1855), Allahabad High Court (1869), Allahabad Public Library (1878), Allahabad University (1887), All-Saints Cathedral Church (1887), and Allahabad Museum (1931) [20]. These edifices feature substantial brick and stone masonry construction but suffer due to inadequate maintenance.

Built in 1915 during the British era, the building, depicted in Fig. 1, features a load-bearing brick masonry structure. Stones were used for support and ornamentation, including plinths, openings, arches, columns, and balconies. Towers, essential structural components, come in diverse cross-sections and heights. These towers throughout the building employ distinct construction methods and geometrical specifications. The SH building is a remarkable example of a load-bearing structure featuring unreinforced brick masonry walls, stone arches, and vaults. The symmetric construction technique on both sides of the central hall showcases Indo-Saracenic architecture. British engineer "Sir Swinton Jacob," known for designing "Victoria-House" in Kolkata, designed the building, which began construction in 1910 and concluded in 1915. Resting on a 1.07 m thick plinth base embellished with stone chips and tiles, the building spans ~ 112.74 m in length and ~ 54.54 m in width. While the floors reach a height of ~ 18.24 m up to the roof, the towers vary from 18.75 m to 30.48 m.

Load-bearing brick walls exhibit varying thicknesses, ranging from 1.5 m to 0.6 m on different floor levels. The building encompasses two stories, with towers commencing from the subsequent floor level. Its distinctive geometric plan features thick masonry walls fringed by stone arches on both sides, separated by rectangular and octagonal columns. Notably, four impressive towers are essential transept elements, incorporating a blend of brick masonry, stone, and timber. The main entrance boasts three distinct entrance porches, each designed with unique geometrical cross-sections and architectural styles. North and South porches share similar parameters and materials, while the East porch showcases a distinct design. This building remains a significant representation of Indo-Saracenic architecture and historical workmanship.

The entire building structure is enveloped in simple cross and barrel vaulting, devoid of decorative elements. Constructed during the British era, the building harmoniously blends Mughal and British architectural styles and construction techniques. Opening its doors in 1915, the building boasts two-floors a year after completion. Ground-Floor (GF) showcases stone arches and panels of varying thicknesses, while first-floor (FF) is exclusively built with brick masonry walls ranging from 0.91 m to 0.48 m in thickness. These brick walls are shielded with approximately one-inch-thick internal plaster, while the exterior remains unplastered, exhibiting a red colour. Over time, the brick surfaces have deteriorated due to exposure to rainwater, moisture, and temperature variations at all levels.

Renovations to the building's first and second-floor (SF) levels have been periodically undertaken. These floor levels are constructed using brick masonry, supported by I-section iron-panels. However, the construction materials have deteriorated, affecting connections and surfaces. Similar I-sections with the exact dimensions are apparent in the longitudinal direction in meeting rooms, examination halls, and rooms, and in the transverse direction in towers, verandahs, and entrance porches. This distributes the superstructure load through the I-section to the masonry wall and gives the upper floor a great deal of support. Central hall's tile floor rests on truss elements in the transverse direction. The building features diverse structural elements, including towers, walls, arches, domes, and façades, as illustrated in Fig. 1. These towers are strategically positioned at corners and midpoints of the building. With over two-hundred arches throughout the structure, the transepts and apse hold significant dimensions in both-plan and height. The ground-floor accommodates three spacious halls- the Examination Hall (EH), Central Hall (CH), and Meeting Hall (MH)-designed for various purposes such as convocations, meetings, conferences, and cultural activities. The CH, with an estimated seating capacity of eight hundred to one thousand people, is the focal point for gatherings. This building has accommodated over a hundred esteemed officials and educators. Towers serve as staircases, clock holders, and architectural features. They are crucial for interconnecting floor levels. This research analyzes stress and deformation responses following visual inspection and non-destructive testing on tower elements. The study uses a 3D-FE model (macro and homogeneous) and experimental mechanical properties to assess tower element behaviour through static and dynamic analyses.

Visual Inspection Survey of the Towers

A comprehensive geometric survey and in-situ assessment, along with consultations with the civil engineer in charge, revealed that the masonry wall thickness ranges from approximately 1.5 m at the ground level to 0.6 m at the first floor. The building prominently features sandstone in architectural elements such as verandahs, entrance porches, staircases, and tower canopies (Fig. 2).

Visual inspection showed widespread structural deterioration, primarily due to long-term exposure to moisture, rainwater seepage, and fluctuating weather conditions. Structural damage is evident in critical components including stone arches, façades, columns, and decorative features. Cracks measuring between 2 and 10 mm were observed in ground and second-floor masonry walls, while major cracks—up to 30 mm—were noted in the stone arches at entrance porches (Fig. 3).

The Side Stair Tower (SST), Front Corner Tower (FCT), and Back Corner Tower (BCT) exhibited severe degradation, particularly on the second floor where both structural and ornamental elements failed. Roof structures also showed major cracking on both inner and outer faces. As a result, access to several parts of the building has been restricted, and all towers are closed to the public except for essential maintenance.

The 2015 Nepal earthquake worsened the condition, causing the collapse of decorative elements in arches and tower tops. Cracks ranging from ~ 1 mm to ~ 30 mm were documented in verandahs, wall openings, and roofing zones. The collapse of plaster due to moisture-induced expansion (intumescence) was widespread.

Roof elements have significantly weakened over time due to ongoing moisture intrusion. In several collapsed portions, horizontally laid bricks indicated poor original bonding. Emergency retrofitting work included concrete plaster overlays, tar-coal waterproofing, and structural reinforcement in high-risk areas as shown in Fig. 3a and b. Cracks around the main door arch and upper stairs still pose serious structural concerns, necessitating urgent intervention.

The tower exhibits strong construction, consistently integrating stone and brick masonry across all levels. Visual assessment reveals the current condition of both the load-bearing and ornamental masonry walls, with particular attention to the integrity of brick-to-mortar bonding. At the ground floor level, the inner load-bearing brick walls display a cellular configuration, characterized by mortar joints approximately 25 mm thick between stretcher and header courses. On the exterior, where no plaster has been applied, the mortar joints range between 10 and 20 mm in thickness.

The upper portions of the tower feature unplastered brickwork laid predominantly in English bond, with a discernible reduction in mortar joint thickness as the elevation increases. Lime-surkhi mortar has been extensively used throughout the structure, serving both bonding and plastering functions. For additional structural stability, the tower corners have been reinforced using stone tiles and chippings.

At the uppermost levels, the masonry incorporates finely dressed stone units aligned with precision and joined by comparatively thinner mortar joints, whereas the ground-level stone masonry exhibits joints approximately 10 mm thick. The continuous use of composite stone and brick masonry at all elevations underscores a unified construction technique. However, prolonged exposure to environmental conditions has led to progressive deterioration in the bonding mortar, indicating a need for conservation intervention.

Fig. 2 Cracks and damages visible in structural elements

Structural Geometrical Cross-Sectional Drawing of Towers

The towers were constructed at different locations within the building. Eleven towers were built, each with varying design parameters, such as style, geometrical cross-sections, heights, and materials. Assessment focused on four specific towers: (1) clock tower (CT), (2) SST, (3) FCT, and (4) BCT, as illustrated in Fig. 4. Each tower features distinct materials and styles tailored to their specific functions within the building. Towers vary in wall thickness (from 1.22 m to 0.31 m), height (18.75 m to 30.48 m), and slenderness ratios. Dome elements at the tops of the towers are constructed in different shapes (circular and rectangular) and sizes. The tower heights range from 18.75 m to 30.48 m, with wall thickness decreasing as height increases.

The wall thickness varies on each floor of the towers, decreasing from 1.22 m at the base to 0.31 m at higher levels, correlating with floor height and openings. Geometric drawings of the towers were based on in-situ surveys. The towers were restricted to the second-floor due to significant cracks and damage in the structural elements and construction materials visible on the upper floors. Each tower's geometric drawings and FE-modeling were individually prepared after visual inspection and assessment. Static and dynamic analyses were conducted according to Indian Standard (IS) codal provisions-and-guidelines [54, 55]. The analysis of all four towers is discussed below:

(a) Materials deterioration of structural elements

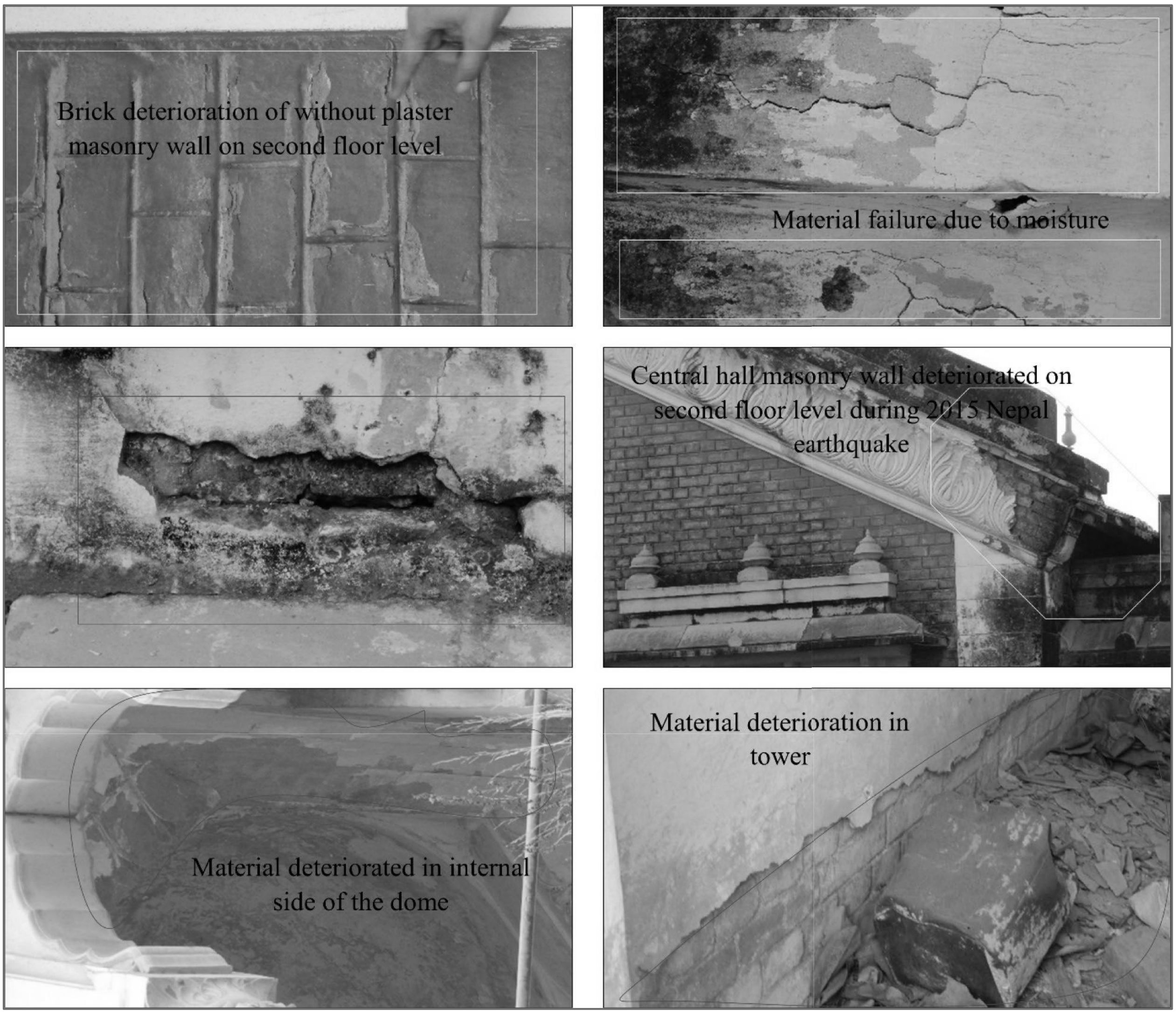

(b) Construction materials deteriorated numerous components.

Fig. 3 Visual inspection survey of the tower

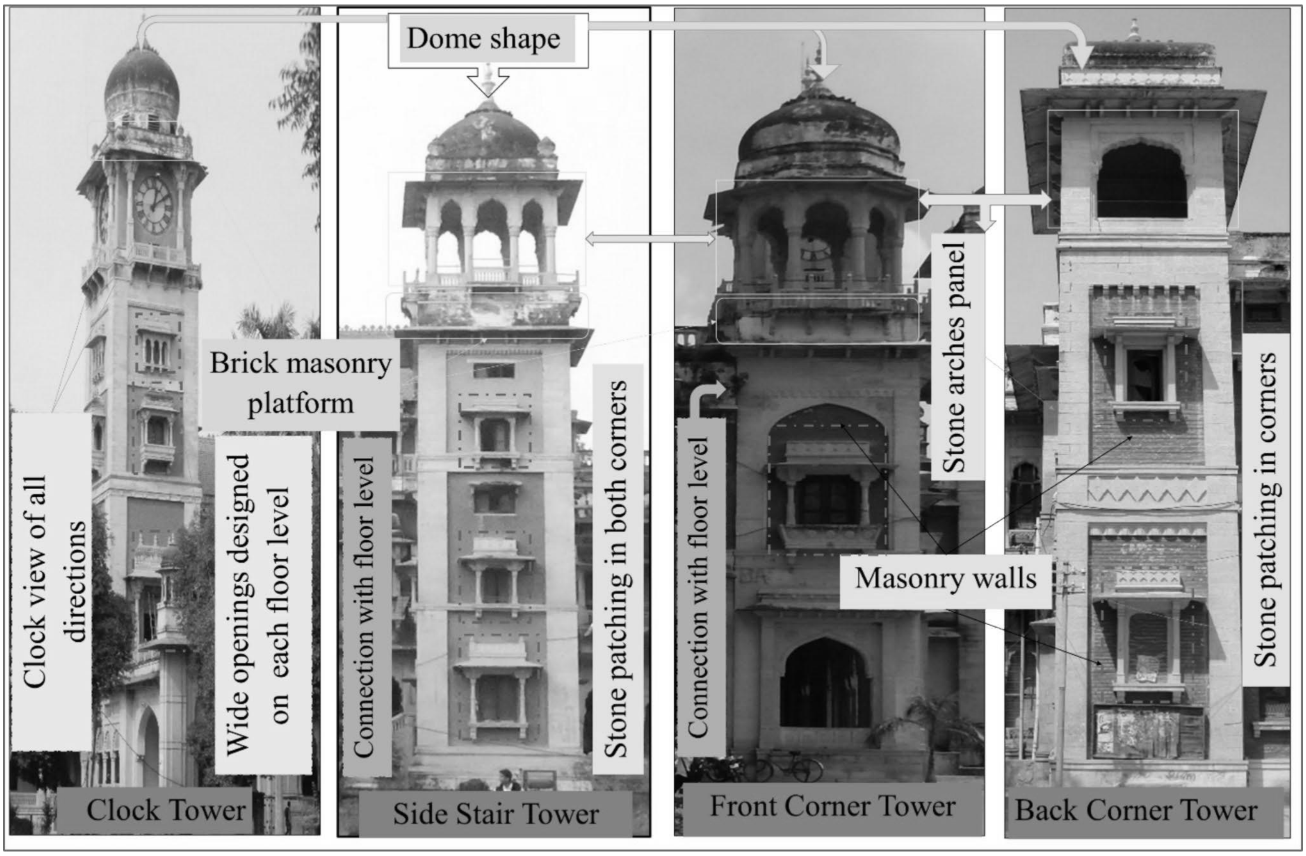

Fig. 4 Structural specification views of tower elements of the building

The geometrical representation of the towers was modelled using data gathered from in-situ surveys and consultations with the Engineer In-charge at Allahabad University. The process began with a geometric study to verify dimensions against existing drawings of the building. Inspections were conducted to understand the geometric dimensions, designs, construction materials, techniques, and initial conditions, including cracks and damages. Measurements were taken using a Disto-meter measuring device and tape, assessing accessible portions and major cracks with a steel scale. Although certain upper portions were inaccessible due to structural failure, measurements were completed using a Disto-meter. Minor decorative components at the inaccessible tops were accounted. Detailed geometrical drawings, in plan and elevation, were produced to scale using AutoCAD, as depicted in Fig. 5. Each tower's unique style, dimensions, and structural components were accurately designed and documented individually.

The Clock Tower (CT), standing 30.48 m high, is one of the tallest and most prominent towers in the building. It is constructed entirely from brick masonry, with stone materials used for structural components, and is located at the front entrance of the building, rising up to six floors. The ground floor cross-section is nearly rectangular and divided into seven distinct parts, including the clock section and dome. The entrance-hall arch extends 0.62 m outside the masonry wall, while the stone arches of the front verandah are recessed 0.7 m inside the CT. The geometric details of the CT have been previously discussed [56]. The Side Stair Towers (SST) are situated on either side of the CT and at each corner of the central hall (CH), mirroring the CT's structural patterns in geometry, material composition, and architectural style. Although now inaccessible due to structural damage and cracks, the SSTs were once connected to the CH's internal porch. The internal masonry walls extend 12.20 m within the verandah. Stone stairs feature a rise of 0.15 m, a tread of 0.38 m, and a width of 1.22 m on the ground and first floors, transitioning to a 0.25 m tread on the second floor. The upper portions of the towers are permanently restricted due to damage, necessitating renovations with new materials. The Front Corner Tower (FCT) is located at the front corner and middle portion of the building, sharing geometric design and structural materials with the other towers. The Back Corner Tower (BCT), fully constructed from brick masonry, features stone arches and panels similar to those in the SST and FCT on the second floor. Figures 4 and 5 illustrate the structural views and AutoCAD drawings,

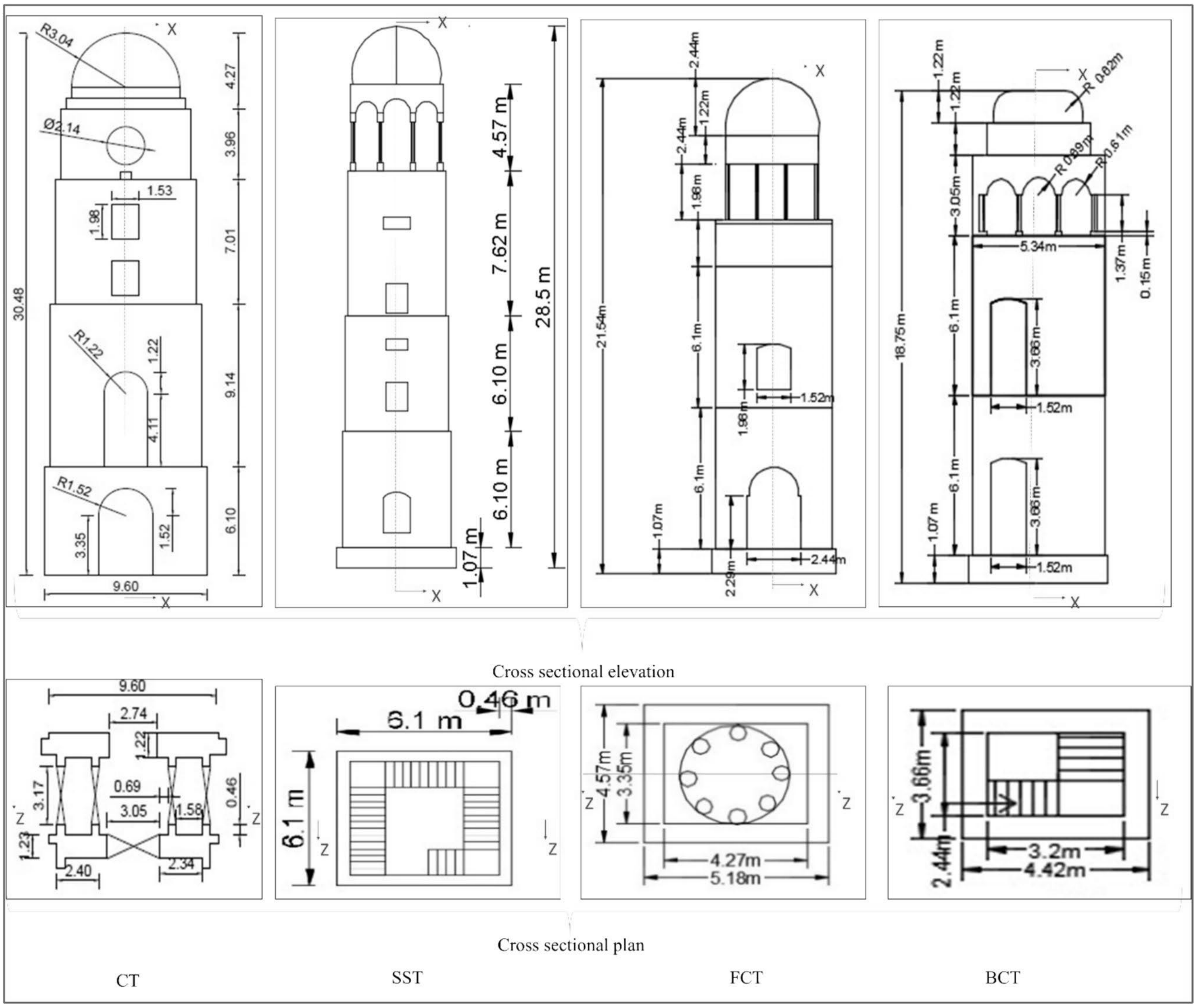

Fig. 5 Geometrical cross-sectional plan and elevation drawing of towers

while Table 1 details the geometric dimensions of structural elements [56–58].

Numerical 3D Finite Element Modelling of Tower Elements

Modeling historical masonry structures presents significant challenges due to various uncertainties. These include a lack of detailed historical records, unknown original geometries, varying materials, and a mix of construction techniques and architectural styles. Over time, these structures also develop cracks, damage, and structural failures due to environmental exposure, previous earthquakes, and aging, adding complexity to the modeling process. In addition, past retrofitting and renovations make it difficult to determine original design intentions. As a result, the Finite Element (FE) modeling of such buildings becomes both time-consuming and technically demanding.

The FE method is a powerful numerical tool used to simulate the structural response of masonry buildings under various loading conditions. Depending on the scale and purpose, researchers generally adopt two main modeling approaches: micro-modeling and macro-modeling, including sub-approaches such as homogenized and detailed unit-based models. Micro-modeling captures each component (brick, mortar) separately, providing high accuracy but at a high computational cost. Macro-modeling simplifies the structure as a homogeneous material, making it ideal for large-scale analysis while balancing accuracy and efficiency.

In this study, macro-modeling with homogenization was employed to simulate the global behavior of a large historic

Table 1 Geometrical structural diamension details of the tower elements

Stuctural elements	Width-w(m)	Initial Height-h(m)	Final Crown Height-H(m)	Length-(m)	Thickness-(m)	Diameter-(m)
Clock tower						
Verandah arch	3.16 m	3.13 m	4.68 m	–	–	–
Entrance hall arch	3.05 m	3.095 m	4.717 m	–	–	–
Plinth level	–	–	1.07 m	–	–	–
Base dimensions	6.6 m	–	–	9.60 m	–	–
Tapering	5.39 m	–	–	8.08 m	–	–
Ventilators	0.31 m	–	0.31 m	–	–	–
Clock portion (Sixth-floor)	5.94 m	–	6.40 m	–	–	–
Clock diameter	–	–	–	–	–	2.14 m
Ground floor arches	3.17 m	–	5.837 m	–	–	–
Openings (FF)	2.74 m	–	4.87 m	–	–	–
Openings (SF)	1.53 m	–	1.98 m	–	–	–
Roof	–	–	–	–	0.31 m	–
Dome	–	–	3.35 m	–	0.31 m	6.08 m
Side stair tower						
Tower height	–	–	28.50 m	–	–	–
Plinth level	7.0 m	–	1.07 m	7.0 m	–	–
GF&FF	6.71 m	–	6.10 m	6.71 m	–	–
SF&TF	6.1 m	–	–	6.1 m	–	–
Front corner tower						
Door opening	1.52 m	–	3.66 m	–	–	–
Window opening	1.52 m	–	1.96 m	–	–	–
Back corner tower						
Tower rectangular base	4.57 m	–	1.07 m	5.94 m	–	–
Door openings GF&FF	1.52 m	–	1.96 m	–	–	–
Window openings GF&FF	0.91 m	–	1.5 m	–	–	–
Rectangular drum height	–	–	1.22 m	–	–	–

masonry building (Fig. 6). The masonry towers, composed of stone and brick, were modeled using a homogeneous material approach. However, critical structural features such as door and window openings, ventilators, and stairwells were modeled separately to preserve geometrical and structural integrity. Most openings were rectangular in shape and were designed symmetrically. Archways with two- and three-hinged profiles, including semicircular arches, were also modeled floor-wise to reflect their in-plane behavior.

For the dome geometry, a revolved modeling approach was used along the vertical axis to accurately capture its twisted, boat-shaped form. The domes were supported by a combination of rectangular, circular, and octagonal panels. Octagonal-sectioned columns were introduced under key arches and dome bases across various floor levels. These details were based on field measurements to preserve architectural fidelity.

The FE simulation excluded non-structural features such as balconies, sunshades, timber floors, and window decorations for simplicity. Nonetheless, the primary load-bearing system including walls, arches, columns, and domes—was modeled in detail. Cracks, localized deterioration, and joint separations were addressed during material property assignment using appropriate assumptions in the homogenization process.

The high-performance computing setup used for modeling consisted of a 2.4 GHz Intel Xeon processor, 24 GB RAM, 2 TB storage, and a 2 GB graphics card, enabling large-scale model simulations with reasonable resolution and convergence time. Meshing involved solid elements and nodes, tailored to capture the structural behavior without over-refining the model (Table 2). This was especially effective in modeling transitions between wall openings and arch supports.

While macro-modeling is not suited for capturing highly localized failures or post-peak softening, it remains efficient for evaluating the global structural response of large, complex masonry structures. The method establishes a practical link between modeled structural response and observed deterioration patterns, helping guide restoration

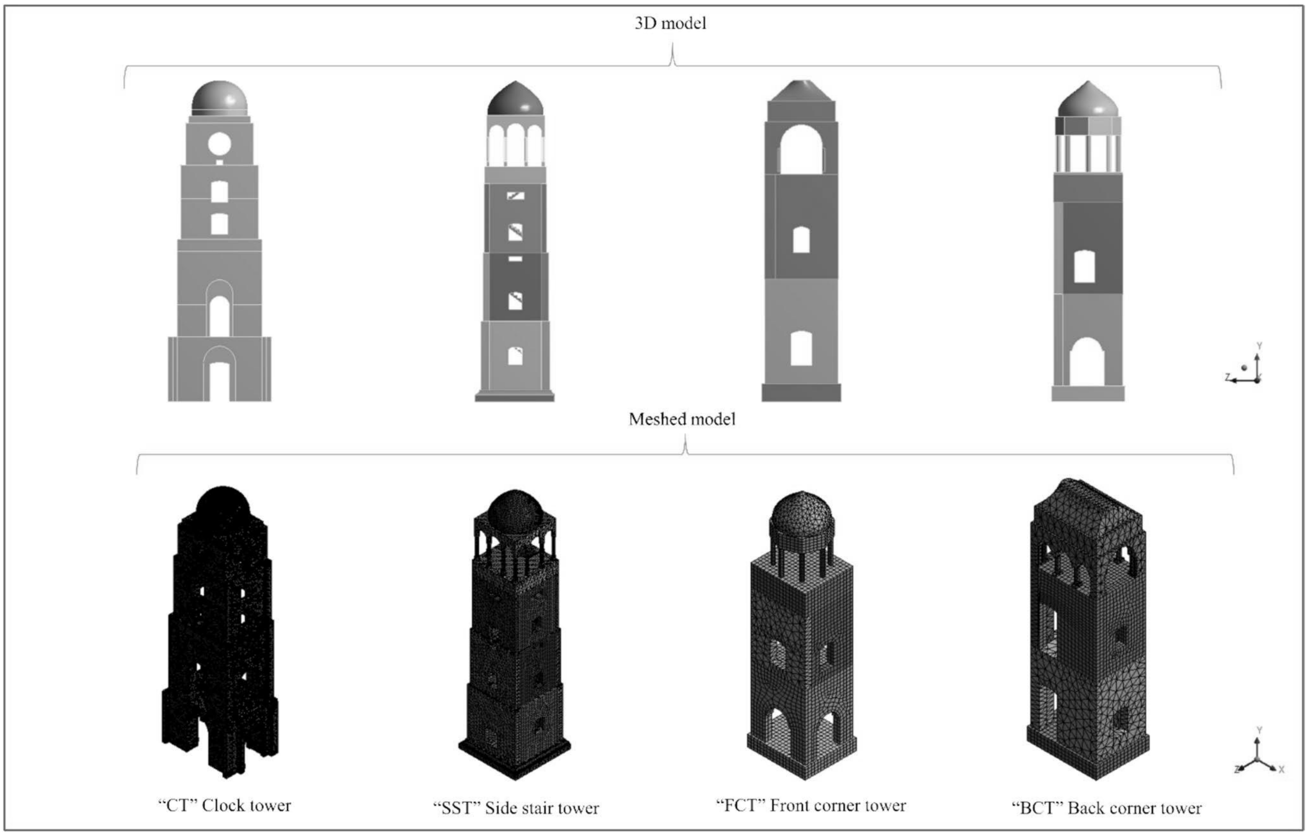

Fig. 6 Finite Element modelling and meshing of the towers

or reinforcement decisions based on realistic simulation outcomes.

The modelling employed various elements: SOLID186 (20-Noded), SOLID187 (10-Noded) 3D-solid elements for masonry walls and stairs, and SURF-154 for the dome. To ensure structural connections, TARGE170 and CONTA174 contacts were integrated [53]. The meshing process generated nodes and solid elements, as indicated in Table 2. This selection was motivated by the elements' ability to exhibit quadratic displacement behaviour and accommodate plasticity, hyper-elasticity, creep, stress stiffening, and large deflections and strains. Prominent tower openings and vaults on each floor were replicated. Notably, specific attention was devoted to accurately modelling the multi-leaf masonry walls at each floor level.

Table 2 Nodes and solid elements during the meshing of towers

Towers	Nodes	Solid elements
CT	184,627	104,037
SST	1,466,852	922,129
FCT	129,971	27,990
BCT	109,647	37,205

Non-destructive Testing

The Rebound Hammer and Ultrasonic Pulse Velocity (UPV) tests present a highly effective, non-destructive methodology for assessing the mechanical properties of masonry, including brick and stone. The Rebound Hammer measures surface hardness to estimate compressive strength, while the UPV test evaluates material integrity by measuring the speed of ultrasonic pulses travelling through the structure, identifying internal defects. When combined, these methods offer a comprehensive assessment by correlating surface hardness with internal uniformity, detecting both surface and subsurface deterioration. Accurate calibration of the specific masonry material is crucial for reliable results, and it has been performed in the laboratory. Together, these techniques significantly improve the evaluation and monitoring of masonry structures, particularly in heritage conservation [59–62]. Standard practices, such as ASTM C805 and IS 516, guide their application in both concrete and masonry assessments (ASTM C805, 2016; Indian Standards 516 Part 5 (Sec-1 2018) and (Sec-4 2020)). There are three methods to evaluate the mechanical properties of materials. Mechanical properties are typically evaluated through destructive testing (DT), minor destructive testing (MDT), and non-destructive testing (NDT). Pérez-Gracia et al. (2013) have utilized MDT and NDT methods to assess these properties, applying Rebound Hammer and UPV tests to tower elements to estimate properties such as density, Young's modulus, and Poisson's ratio in consistent locations across the structure [63].

Rebound Hammer (RH) Test

Rebound Hammer test has been performed on load-bearing masonry wall elements of the tower's elements at numerous locations selected with and without plaster. The initial testing was conducted at sixteen points at each respective location. The testing was performed on plastered "RH-P" and without plastered "RH-WoP" masonry walls of different locations in the tower, which are free from cracks and damages, seepage and moisture, and other impurities. RH testing was performed using the Indian-code [64] for the actual procedure and guidelines. First, the RH testing was performed on the plastered masonry wall at the second-floor level. Ten testing locations have been identified as T-RH-P-1 to T-RH-P-10, respectively, T-MW-P as indicated by Tower-Masonry Wall-Plaster. The RH values have been obtained on the tower's sixteen points of plaster masonry wall, as shown in Table 3. The test has been performed at different locations on the wall. The maximum and minimum average RH index values observed on locations T-RH-P-3 and T-RH-P-6 were 27.56 and 21.34, respectively.

RH testing has been completed on the plastered brick masonry wall elements of the tower, as shown in Fig. 7. The testing locations have been marked on the different points shown in Fig. 7a. After analyzing the experimental data of the RH index, the compressive strength has been obtained between 24 to 25 MPa of the plastered masonry walls. The compressive strength of plaster walls and RH test locations have been visualized in ten locations of the tower, as shown in Fig. 7b. In the testing, the masonry walls of the tower have observed the compressive strength as well as good due to 25 mm thick plaster material through the internal side.

RH testing was conducted on the unplastered ("WoP") brick masonry walls of the tower elements at the first and second-floor levels. These tests were performed on the external sides of the tower elements, presenting challenges in selecting appropriate testing locations. The outer surfaces of these tower elements are directly exposed to weather and atmospheric conditions, including temperature variations, rainwater, seepage, and moisture, all of which contribute to the deterioration of brick materials and the formation of cracks. These factors also affect the colour of the masonry.

Conducting RH tests on the external side was particularly difficult due to the need to identify optimal testing locations, such as the bottom of the porch and the back side walls of the tower. The WoP walls were tested using the same parameters applied to the plastered masonry walls of the tower elements. RH testing was performed at ten locations on the towers, as detailed in Table 4. The testing locations on the unplastered masonry walls of the side stair tower and clock tower at the second-floor level are identified as T-RH-WoP-1 to T-RH-WoP-10.

After the testing, the maximum and minimum RH-index of WoP masonry walls were 58.25 and 46.31 at locations T-RH-WoP-4 and T-RH-WoP-10, respectively. The compiled testing locations and results of the without plaster walls are shown in Fig. 8. The testing locations have been marked at approx.-1 m height on the walls shown in Fig. 8a. The RH-index response is the without-plaster walls surface response of the tower walls after using the linear correlation (Eq. 1) to convert the surface RH-index to the compressive strength of the WoP masonry walls of the towers. The compressive strength has been observed at a maximum of 24.13 MPa and a minimum of 15.62 MPa at locations 4 and 10, respectively. The average compressive strength observed on the WoP masonry wall is approximately 20 MPa of the entire testing location of the walls. The intensity of the compressive strength has decreased as compared to plaster walls.

$$\text{Linear formulation} = 0.713 * \left(S_3\right) - 17.4 \quad (1)$$

Table 3 RH testing of plaster masonry wall elements

Location	Rebound hammer index																Average
T-RH-P-1	29.5	19.5	24.5	16.5	19.5	27.5	20.4	18.5	32.5	19.5	18.5	30.5	20	20	23.5	26.5	22.93
T-RH-P-2	16	26.5	16	24	23	32.5	24	22.5	27	16.5	16	32.5	24.5	24.5	30.5	18	23.38
T-RH-P-3	28.5	36	32.5	23.5	28.5	28	23.5	26	28	26	22	23	28	29	36.5	22	27.56
T-RH-P-4	18.5	20	26	17.5	19	26	20.5	23.5	19.5	29.5	28.5	24.5	26.5	32	19	23.5	23.38
T-RH-P-5	27	19	14	32.5	27	24.5	19	21	30.5	32	26.5	19.5	29	31.5	24.5	26.5	25.25
T-RH-P-6	22.5	26.5	24.5	21	18.5	24	23.5	18.5	18	16.5	20	18	25.5	22.5	26	16	21.34
T-RH-P-7	36	31.5	27	23.5	22	27.5	27.5	28	32.5	20.5	24.5	20.5	26.5	34	34	19	27.16
T-RH-P-8	24.5	29	30.4	19.5	33.5	29.5	28	30.5	19.5	24.5	26	23	24	23.5	26.5	26.5	26.15
T-RH-P-9	20	28.5	23	26.5	25.5	18	24.5	16	20.5	21	23.5	16.5	28	24.5	29	26	23.19
T-RH-P-10	24.5	16.5	23	22.5	30	28	23	19.5	24	26.5	22	19	26.5	22	24	18	23.06

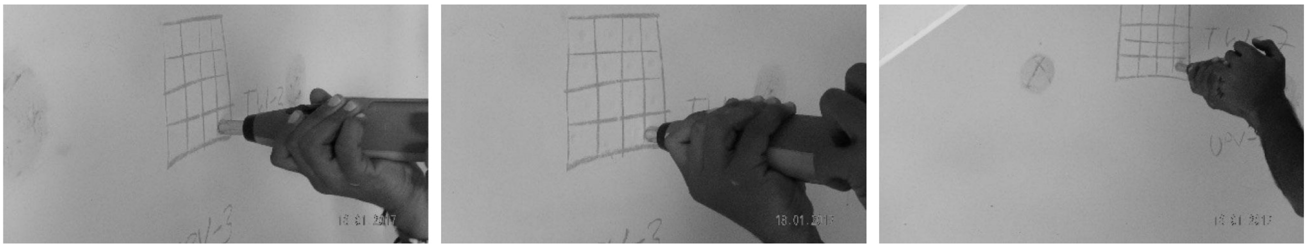

(a) Rebound Hammer testing on the masonry wall of the clock tower

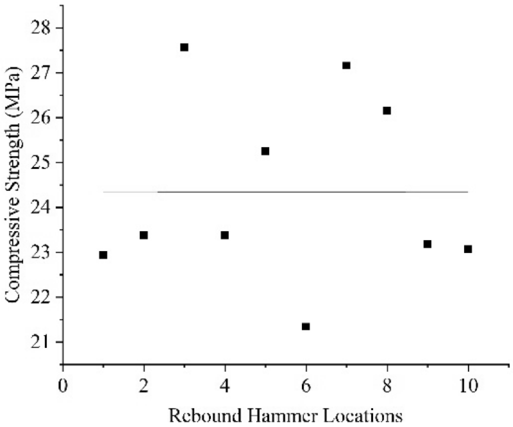

(b) Relationship between compressive strength and RH Index

Fig. 7 Testing locations and average compressive strength

Table 4 RH testing on "WoP" masonry walls

Location	Rebound Hammer Index																Average
T-RH-WoP-1	43.5	49	37.5	43	52.5	54	56.5	61	40.5	54	53.5	46	47.5	53.5	40	48	48.75
T-RH-WoP-2	53	40.5	52	61	50.5	52.5	67	59.5	48.5	48	60	62	63.5	62	58.5	59.5	56.13
T-RH-WoP-3	50	67.5	48.5	50.5	56	56	52.5	62.5	67	52	58.5	56.5	68.5	68.5	54.5	46.5	57.22
T-RH-WoP-4	67	63.5	64.5	64	48.5	64.5	64	63	58.5	52.5	56	60.5	48.5	51	46	60	58.25
T-RH-WoP-5	62.5	56	39.5	54	60.5	42.5	51.5	56	50	51	42	58.5	46	46	45	49	50.63
T-RH-WoP-6	64	43	58	41.5	47	61	48.5	43.5	60.5	46.5	65	61	51.5	44	52.5	56.5	52.75
T-RH-WoP-7	48.5	48.5	52.5	46.5	61	52	39.5	39.5	52.5	60	53.5	49.5	55	48.5	65.5	44.5	51.06
T-RH-WoP-8	54.5	46.5	56	52.5	52.5	49.5	46	48.5	53	54.5	61.5	48.5	46.4	52.5	41	58	51.34
T-RH-WoP-9	54	48.5	47.5	62	52	51.5	49.5	46	51	56.5	54	47.5	49	53.5	48	43	50.84
T-RH-WoP-10	39.5	43	36.5	51.5	46.5	48	42	47.5	52.5	49	39.5	47	51	52.5	47	48	46.31

RH test was performed on stone elements from the ground floor to the top of the tower. In visual inspections, the stone elements are mostly used for decorating and supporting purposes, and they are used in respective dimensions for load-bearing elements. Conducting non-destructive testing is impossible; only load-bearing elements have been selected for RH and UPV testing. The testing was performed on the ground-floor, first-floor and second-floor arch panels of all respected towers. The ground-floor portion of the CT and FCT have been built from the same structural components of fully stone materials. CT has been built with a combination of four arches of similar geometrical dimensions. However, the FCT has been designed using similar construction techniques and different structural element dimensions.

The testing location has been selected in the middle of the arch column at the 1 m to 1.5 m height of the base level of the all-respected floor. During the testing, locations are noted for "T-S," such as T for tower and S for stone. The RH value was between 55 and 90 in the testing on stone elements. The

(a) Identified locations of WoP masonry walls

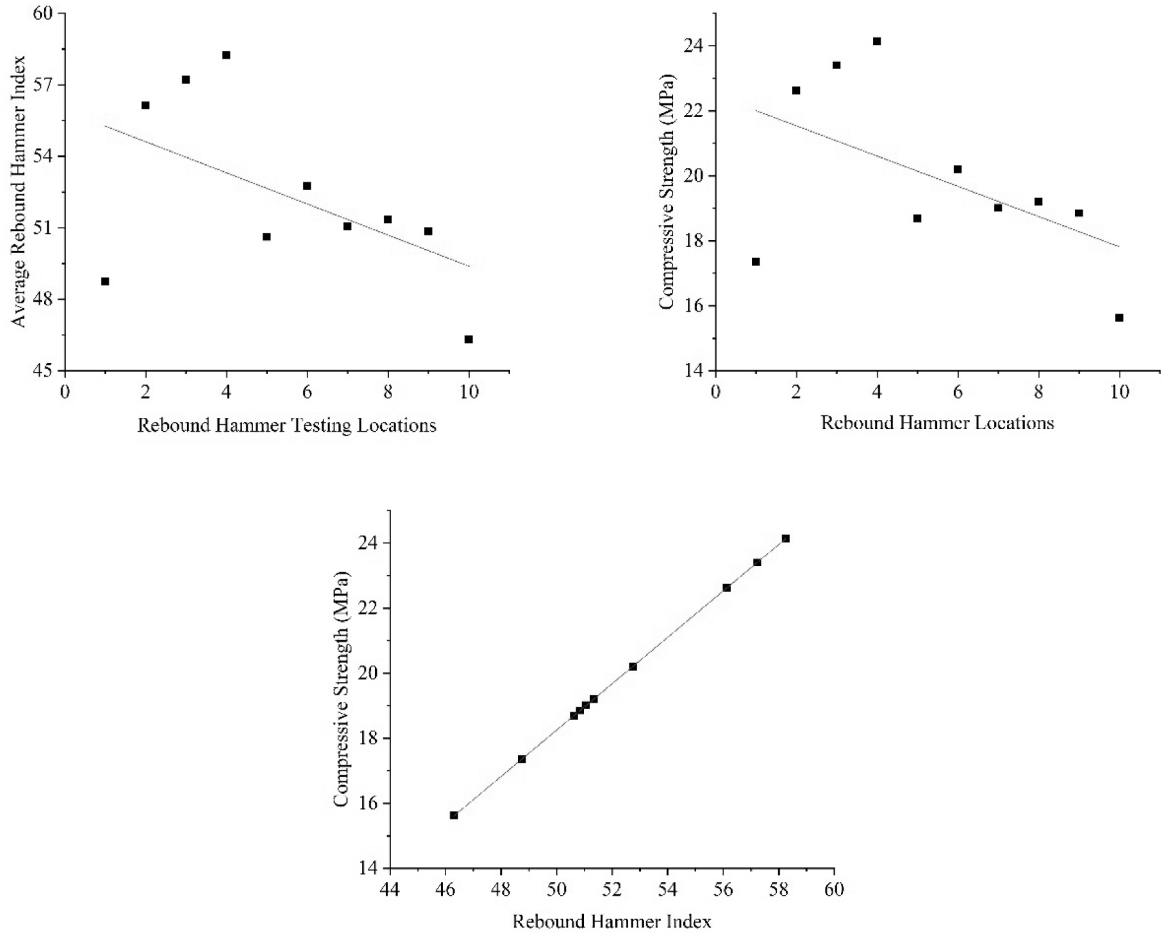

(b) Correlation between RH index and compressive strength

Fig. 8 RH testing on WoP masonry walls of tower elements with relationship b/w RH index and compressive strength

RH-index of the stone arch is shown in Table 5. Only after calibration in the laboratory test, the compressive strength has been evaluated using linear relation, as shown in Eq. 1. The relationship between the average RH-index and compressive strength stone material is shown in Fig. 9.

After the testing has been done on the ten different locations of the arch-columns and façades of the tower elements, as shown in Fig. 9a. The average RH-index has been observed as a maximum of 73.97 and a minimum of 64.71 at locations T-S-9 and T-S-3, respectively. In these similar locations, the compressive strength has been observed at a maximum of 35.34 MPa and a minimum of 28.74 MPa, respectively. All these locations have observed the tower elements' average compressive strength of the stone material of 32.87 MPa. Figure 9b shows the relationship between the average RH-index and compressive strength in testing locations. Finally, the resulting values between compressive strength and RH-index of the stone material are plotted.

Table 5 RH testing on stone elements

Location	Rebound Hammer Index																Average
T-S-1	58	60	73.5	76	64.5	62.5	71.5	67	65	73.5	67	70	58.8	68	66.5	73.5	67.21
T-S-2	68	68	67	74	65.5	73.5	72.5	76	77	79	75	76	73.5	69	77	74.5	72.84
T-S-3	60.5	58	67	67	67.5	68	64.5	67.5	64	66.5	64.5	68.8	62.5	65.5	60.5	63	64.71
T-S-4	72	75	62.5	72.5	60	67	62.5	78.5	69	67.5	63.5	76	75.5	77.5	68.5	69	69.78
T-S-5	64.5	65.5	70.5	74.5	61.5	71.5	80	80.5	70.5	74	76	74	78.5	79	74.5	78	73.31
T-S-6	58.5	70.5	72.5	61	72.5	69.5	79.5	74.5	76	76	66.5	77.5	68	80	73	71.5	71.69
T-S-7	67	68	68.5	67	68.5	80.5	80	69.5	61.5	76.5	76.55	76.5	70.5	81.5	80.5	67	72.47
T-S-8	63.5	60	67	65	72	67.5	67	74	60	64	68.5	62.5	59.5	69.5	67.5	62.5	65.63
T-S-9	74.5	72.5	74	72	69.5	78.5	67.5	76.5	72.5	81.5	78.5	73.5	72.5	73.5	77	69.5	73.97
T-S-10	71	73	68	66.5	77.5	60.5	81.5	77.5	76.5	76.5	76.5	68.5	74	78	78	70.5	73.38

Ultrasonic Pulse Velocity (UPV) Test

The ultrasonic pulse velocity test has been performed on old and new structures to evaluate the mechanical properties of such materials. It is performed on similar locations of the structural elements, where the RH tests the masonry walls and stone elements. Due to the accessibility of the specimen for testing, UPV has been performed using three methods: direct, semi-direct, and indirect procedures [65]. In tower elements, the indirect procedure has been applied to both plastered and un-plastered masonry walls at ten different locations (UPV-S-L1 to UPV-S-L10), maintaining the same path-length between the transducer and receiver. The path length has been set to 0.5 m for all the testing locations of brick and stone elements of the towers. The pulse velocity was obtained from [66], and accurate testing procedures and guidelines were obtained during the testing. The testing locations were thoroughly cleaned during the testing. Grease was used as a lubricant to smooth the pulse response between the transducer and the receiver. The pulse velocity has been observed at a maximum of 2.427 km/sec and a minimum of 1.086 km/sec at the locations of S-L10 and S-L6, respectively. The testing location of the masonry walls with path-length, travel-time and pulse velocity of the tower as shown in Table 6. The UPV testing locations of walls and the relationship between pulse velocity and Young's modulus are shown in Fig. 10.

The testing has been done successfully on the selected UPV test locations of tower elements of plastered and without plastered brick masonry walls on the GF and SF-level, as shown in Fig. 10a. The entire locations with pulse velocity responses of the wall elements have shown in Fig. 10. The pulse velocity has been observed average 1.2 km/sec to 1.6 km/sec for all the locations of brick masonry walls for plaster and without plaster materials. The young's modulus of brick masonry walls element has been observed for dynamic range as 2000 MPa to 12000 MPa and static 1000 MPa to 5000 MPa, respectively as shown in Fig. 10b. The young's modulus has been evaluated the average for the static as 2956 MPa for all types of brick masonry walls of the tower elements.

The masonry wall testing was completed, after which the focus shifted to the stone elements of the columns and façades of the towers. UPV testing was conducted on the stone arch of the CT, FCT on the GF, and the BCT on the SF. This testing utilized semi-direct and direct methods to measure the travel time and pulse velocity over a 0.5 m path-length between the transducer and receiver. Testing was primarily conducted on the columns of arches, though façades were also evaluated, revealing minor cracks, moisture, and deterioration of the stone material. UPV testing locations on the stone arches' columns were designated as S-L-1 to S-L-10 for semi-direct testing and D-L-1 to D-L-10 for direct testing. The locations and testing values of the entrance arch are detailed in Table 7.

The relationship between pulse velocity and Young's modulus of direct and surface test is shown in Fig. 11. The average pulse velocity has been observed for surface and direct testing as 2.4 km/sec and 2.69 km/sec and static Young's modulus for 6117 MPa and 8606 MPa as shown in Fig. 11b. After the testing, the average pulse velocity has been observed more in the stone elements as compared to masonry. The stone elements have been exposed in the building from plaster masonry walls; however, most of the deterioration is visible in these elements. Finally, all the experimental results of the testing were used for tower analysis, with the masonry and stone elements assigned accordingly.

Static and Dynamic Analysis

Static and dynamic analyses were conducted on four distinct towers within the SH building, incorporating a blend of masonry and stone materials. The assessment encompassed standard-gravity and live-load analyses with a fixed base configuration. These evaluations adhered to Indian guidelines featuring seismic provisions. Gravity and live load analyses adhered to the specifications outlined in the Indian

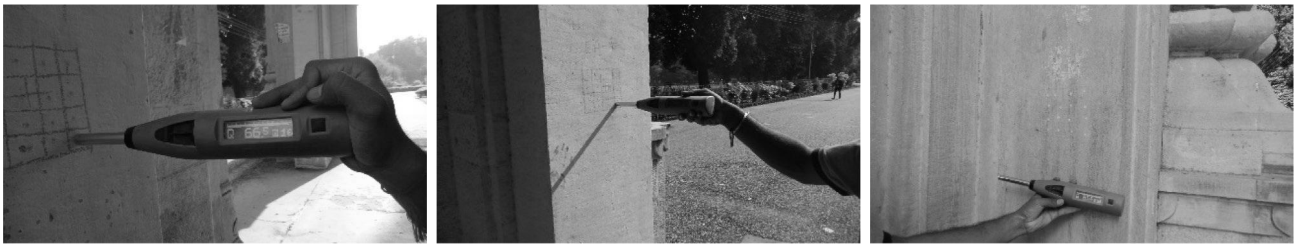

(a) RH testing location of stone elements of tower

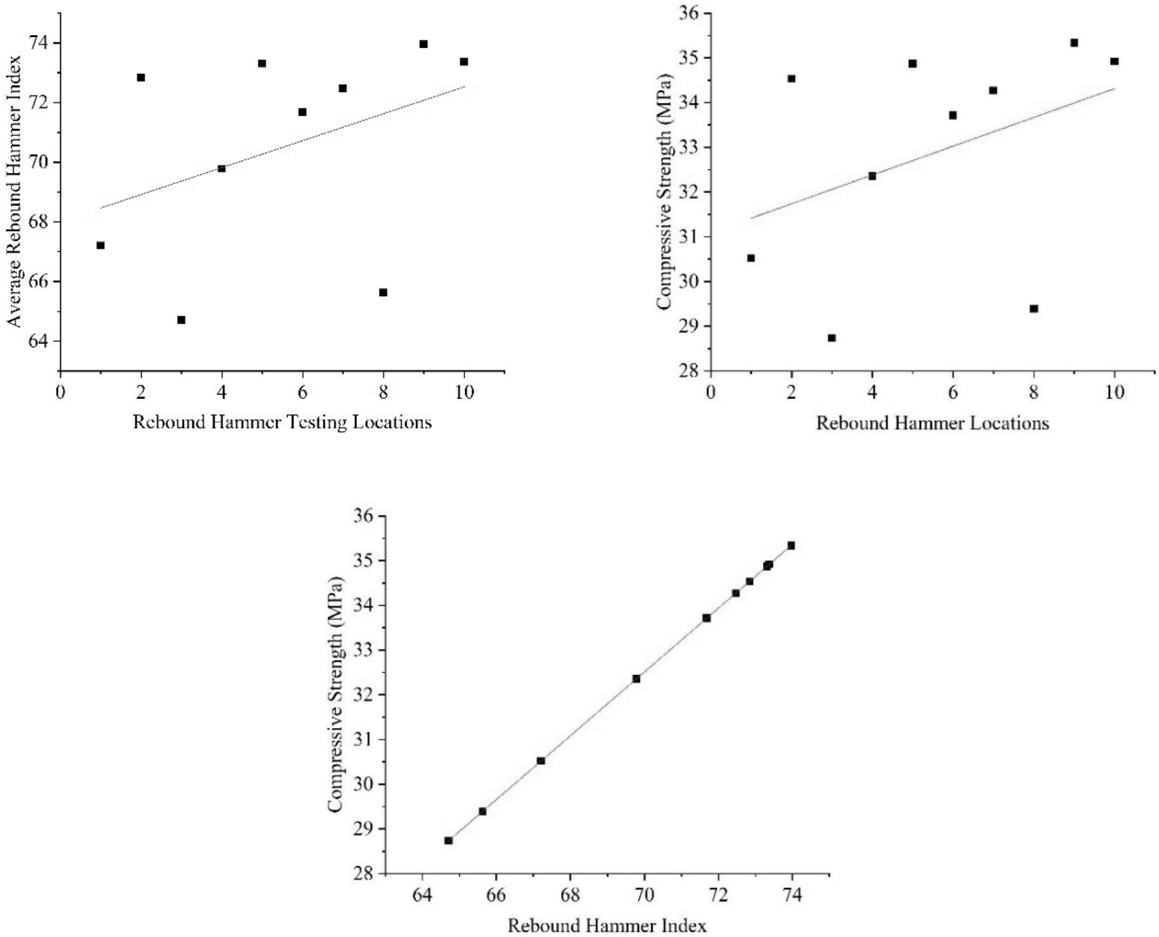

(b) Relationship between RH-index, compressive strength and locations

Fig. 9 RH testing of the stone element of tower components

standard codes IS:875 Part-1&2 [54, 67]. Modal analysis was performed according to IS:1893 (Part-1) 2016, which pertains to the seismic guidelines within the Indian standard code [68]. This analysis yielded six-mode shapes for each tower and their corresponding natural frequencies for four towers.

The investigation incorporated pertinent mechanical properties, including density, Young's modulus, and Poisson's ratio, as parameters for experimental building tests. The material attributes of brick masonry and building stones were assessed using non-destructive testing, the findings of which are summarized in Table 8. Dynamic time history analysis was executed individually for each tower. Ground motion acceleration was simulated for Allahabad city utilizing the EXSIM software, accounting for regional parameters such as fault length, stress drop, and slip distance. This comprehensive analysis encompassed the assessment of acceleration, deformation, and stress responses on every floor of the

Table 6 Indirect UPV testing on without plaster masonry wall elements

UPV location	Path-length [m]	Travel Time [μ Sec]	Pulse velocity [km/sec]
UPV-S-L1	0.5	308	1.623
UPV-S-L2	0.5	267	1.873
UPV-S-L3	0.5	426.5	1.172
UPV-S-L4	0.5	368.5	1.357
UPV-S-L5	0.5	287	1.742
UPV-S-L6	0.5	460.5	1.086
UPV-S-L7	0.5	305	1.639
UPV-S-L8	0.5	275	1.818
UPV-S-L9	0.5	284.5	1.757
UPV-S-L10	0.5	206	2.427

towers. The time history analysis identified critical locations and potential failure points within the towers.

Formulation of von-Mises stress

The von-Mises stress mechanism of the linear analysis is used to determine the stress distribution in the clock tower. Mathematically, the criterion is expressed as:

$$J_2 = k^2 \tag{2}$$

k = the yield stress of the material in pure shear.

$$\sigma_v = \sigma_y = \sqrt{3J_2} \tag{3}$$

σ_y = the yield strength of the material.
σ_v = von-Mises stress

$$\sigma_{\text{von mises}} = \sqrt{\frac{1}{2}\left(\sigma_x - \sigma_y\right)^2 + \left(\sigma_x - \sigma_z\right)^2 + \left(\sigma_y - \sigma_z\right)^2 + 3\left(\tau_{xy}^2 + \tau_{xz}^2 + \tau_{yz}^2\right)} \tag{4}$$

$$\sigma_{\text{von mises}} = \sqrt{\frac{1}{2}\left(\sigma_1 - \sigma_2\right)^2 + \left(\sigma_1 - \sigma_3\right)^2 + \left(\sigma_2 - \sigma_3\right)^2} \tag{5}$$

Site-specific Dynamic Time History Analysis

Due to the non-availability of strong motion data for Allahabad city, a synthetic ground motion was simulated using Boore's stochastic method [69]. The target ground motion amplitude spectrum, which depends on magnitude, distance and duration properties, is given by [70],

Fig. 10 Indirect UPV testing locations with young's modulus and Pulse velocity of masonry walls of tower elements

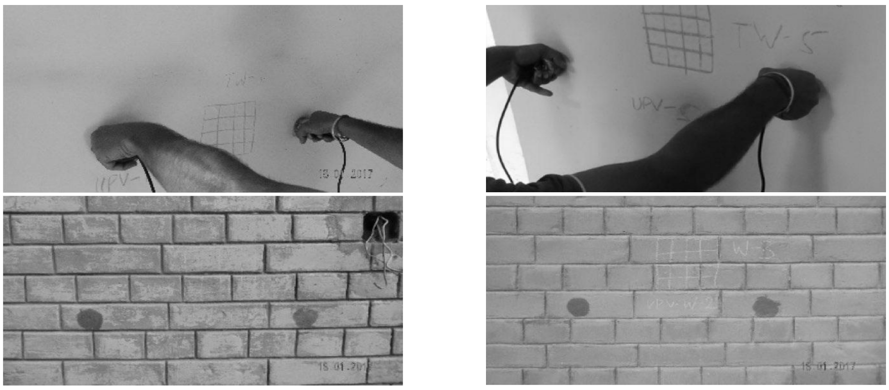

(a) UPV test on "WP" and "WoP" brick-masonry walls of towers

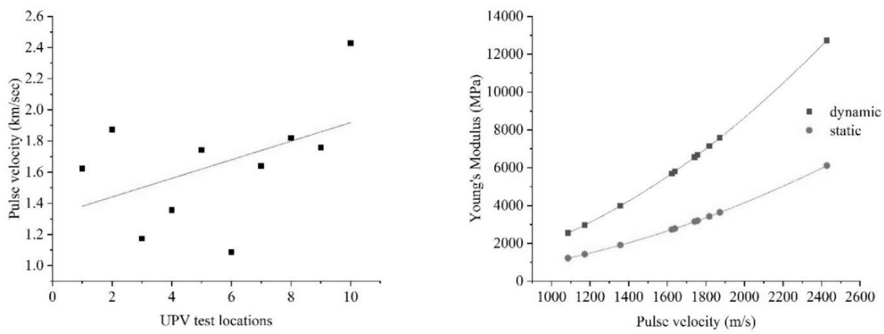

(b) Relationship between pulse velocity and young's modulus

Table 7 UPV surface and direct testing on arch columns of stone elements

UPV location	Path-length [m]	Travel Time [μ Sec]	Pulse velocity [km/sec]
Surface-reading (0.5 m), stone arch			
UPV-S-L1	0.5	221.5	2.257
UPV-S-L2	0.5	218.2	2.291
UPV-S-L3	0.5	202	2.475
UPV-S-L4	0.5	156	3.205
UPV-S-L5	0.5	208.6	2.397
UPV-S-L6	0.5	235.5	2.123
UPV-S-L7	0.5	278	1.799
UPV-S-L8	0.5	205	2.439
UPV-S-L9	0.5	198.5	2.519
UPV-S-L10	0.5	196	2.551
Direct-reading (0.5 m), stone arch			
UPV-D-L1	0.5	255.4	1.958
UPV-D-L2	0.5	262.3	1.906
UPV-D-L3	0.5	261.5	1.912
UPV-D-L4	0.5	212.1	2.357
UPV-D-L5	0.5	212.5	2.353
UPV-D-L6	0.5	94.5	5.291
UPV-D-L7	0.5	165	3.030
UPV-D-L8	0.5	146.5	3.413
UPV-D-L9	0.5	165.5	3.021
UPV-D-L10	0.5	295	1.695

$$A_j(r,f) = \frac{R_{\theta\phi}.F.V}{4\pi\rho v_s^3}.(2\pi f)^2.\frac{M_{0ij}}{\left[1+\left(\frac{f}{f_{0ij}}\right)^2\right]}.G.e^{\frac{-\pi f r_{eff}}{v_s Q(f)}} e^{-\pi k f} \tag{6}$$

where $A_{j(r,f)}$ represents the target amplitude spectrum corresponding to distance (r) and frequency (f), $R_{\_\theta\phi}$ is the radiation pattern constant (typically averaging 0.55 for shear waves), F denotes the free surface coefficient (typically taken as 2), V stands for the partitioning coefficient of shear waves into two components (usually taken as $\sqrt{2}$), ρ denotes the density of rock at the source (fault), v_s signifies the shear wave velocity at the source, M_0ij signifies the seismic moment associated with the ij^{th} sub-fault, $f_{\_0ij}(t)$ denotes the corner frequency linked to the ij^{th} sub-fault at time t, N_r(t) denotes the number of ruptured sub-faults at time t, $M_{\_(0,avg)}$ represents the average sub-fault moment due to each fault, calculated as M/N, where N is the total number of sub-faults. Additional parameters include G, the geometrical spreading function; r_{eff}, the effective distance of the sub-fault from the site; Q(f), the quality factor at frequency f; and k, the high-frequency diminution filter. Prior works have detailed these parameters [71–76]. The time history responses generated for the Allahabad fault are depicted in Fig. 12, featuring a peak ground acceleration (PGA) of 64.21 cm/sec2.

Formulation of Dynamic Time History Analysis

The behaviour of stone arches was examined through stochastic dynamic time history analysis within the context of Allahabad city. The dynamic time history approach utilizing a multi-degree-of-freedom system is presented [7, 77]. The modal matrix for the equation of motion for a multi-degree-of-freedom system in a matrix form can be expressed as

$$[m]\{\ddot{x}\} + [c]\{\dot{x}\} + [k]\{x\} = -\ddot{x}_g(t)[m]\{I\} \tag{7}$$

$[m]$= Mass matrix; $[k]$=Stiffness matrix; $[c]$=Damping matrix; $\{I\}$= Unit vector; $\ddot{x}_g(t)$= Ground acceleration

Coupling of the variables {x} in the physical coordinates may be related with normal or principal coordinates {q} from the transformation and [∅] = the modal matrix

$$\{x\} = [\varnothing]\{q\} \tag{8}$$

$$[M]\{\ddot{q}\} + [C]\{\dot{q}\} + [K]\{q\} = \left\{P_{eff}(x)\right\} \tag{9}$$

$$\left\{P_{eff}(t)\right\} = \left(-\ddot{x}_g(t)[\Phi]^T[m]\{I\}\right) \tag{10}$$

[M], [C] and [K] are the diagonalized modal mass matrix, modal damping matrix, and modal stiffness matrix, respectively, and $\left\{P_{eff}(t)\right\}$ is the effective modal force vector.

Effective force vector

$$\left\{P_{eff}(t)\right\} = \left(-\ddot{x}_g(t)[\Phi]^T[m]\{I\}\right) or \left(-\ddot{x}_g(t)\Gamma_r\right)$$

$$\Gamma_r = \frac{\{\Phi\}_r^T[m]\{I\}}{\{\Phi\}_r^T[m]\{\Phi\}_r} = \frac{\{\Phi\}_r^T[m]\{I\}}{M_r} \tag{11}$$

Displacement response in physical coordinates

$$\{x(t)\} = \sum_{r=1}^{n}\{\Phi\}_r q_r(t) \tag{12}$$

Effective earthquake response force at each storey

$$F_s(t) = [k]\{x(t)\} \tag{13}$$

Results and Discussion

Dead and Live Load Analysis

While earlier studies on historical structures have focused primarily on self-weight and seismic loads, they often overlook live loads. This study emphasizes gravity analysis

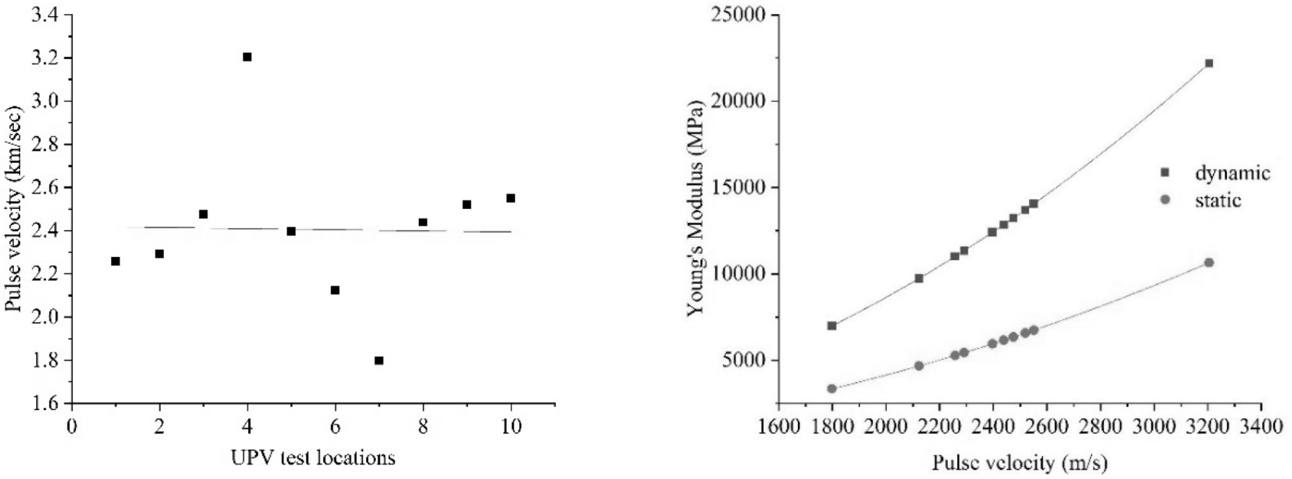

(a) Pulse velocity and young's modulus during surface procedure

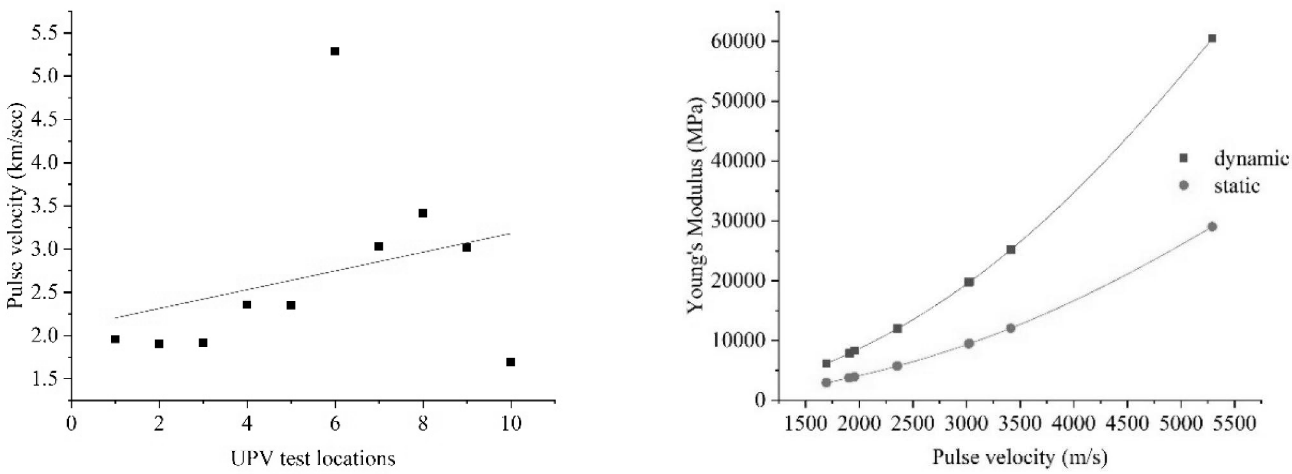

(b) Pulse velocity and young's modulus during direct procedure

Fig. 11 Young's modulus of the stone element of the CT

Table 8 Material properties of tower elements

Structural Materials	Density-(kg/m^3)	Young's modulus-(MPa)	Poisson's-ratio
Masonry	1900	2100	0.2
Stone	2800	3500	0.2
Roof	1900	2100	0.2

to assess maximum stress and deformation in each tower structure. The von Mises stress and deformation results are illustrated in Fig. 13a. In the Central Tower (CT), the ground floor (GF) roof shows the highest stress at 1.88 MPa, while the top of the dome exhibits maximum deformation of 3.98 mm. Minor stresses are distributed along the masonry walls from the ground to the first floor, with higher concentrations near openings such as windows and doors. Significant deformation vectors are observed at the dome and dome base junction. In the Side Stair Tower (SST), the highest stress, 6.26 MPa, is found at the GF stair-to-wall junction, with dome deformation peaking at 4.15 mm. For the Front Corner Tower (FCT), the second-floor octagonal column joints register 2.16 MPa stress, and the dome deforms by 2.56 mm. In the Back Corner Tower (BCT), the GF arch base experiences 0.74 MPa, and the dome's stone panel deforms by 1.92 mm.

Visible cracks and internal deterioration have been observed in the walls, arches, and staircases, particularly above the first floor. Due to structural issues, access to the

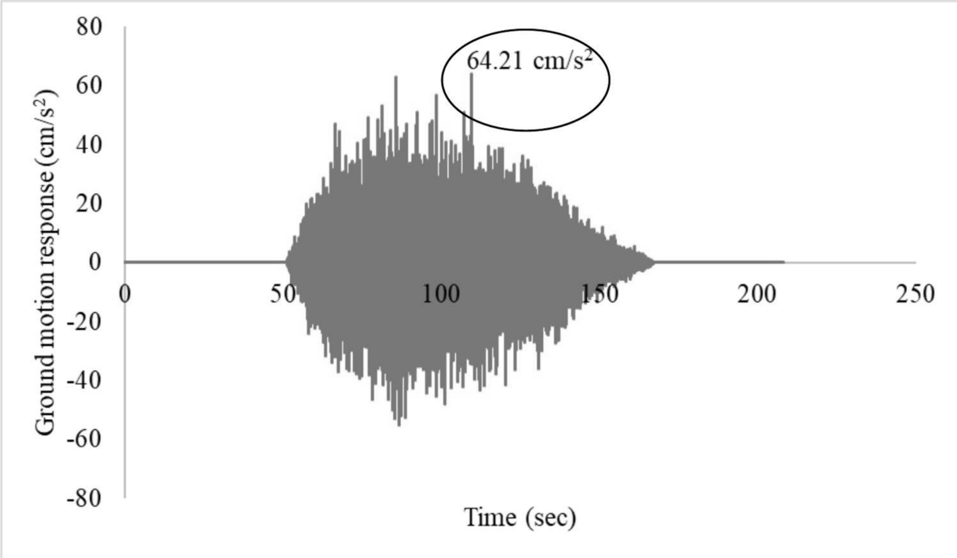

Fig. 12 Synthetic ground-motion of Allahabad city

third floor is currently restricted, although the towers are temporarily reopened during SH building maintenance activities. Stress concentration is highest at the tower base, consistent with the crack patterns shown in Fig. 3. This is expected due to the structural layout, which includes multiple openings on the first and second floors. Maximum stresses occur in the first-floor masonry wall, the center of the arches, and near staircase openings, where stress is significantly concentrated. The first-floor vault, as seen in Fig. 3a and b, shows early signs of stress accumulation. Additional stress develops in the lower slab of the stairs connecting the second and third floors. Minor cracks also appear along the underside of the third-floor stairs, especially near closely spaced walls. Although minor stress zones are noted in the self-weight analysis, pronounced stress responses occur around the openings across all towers. The dome structure behaves well under gravity loads, with a maximum deformation of 0.54 mm at its top and 0.2 mm at the first floor. Figure 13 illustrates the total deformation distribution across all tower levels, supporting these findings..

The live load [67] analysis of the towers reveals stress and deformation responses, as illustrated in Fig. 13b. Within CT, the highest stress of 2.09 MPa and maximum deformation of 4.58 mm are observed at corresponding locations during the live load assessment. SST exhibits a peak stress of 6.34 MPa at the ground to first-floor connection and a maximum deformation of 4.19 mm at the northern stone panel. FCT records maximum stress of 2.39 MPa at a consistent location during gravity loading, accompanied by a peak deformation of 2.88 mm on the octagonal stone panel. In BCT, the highest stress of 0.75 MPa and maximum deformation of 2.03 mm are registered at similar locations during gravity loading. Maximum stress occurs at ground-floor and first-floor openings, encompassing masonry walls and stone panels. These stress responses mirror the gravity loading response at corresponding locations for each tower. In terms of stress, connections between the second and third-floors exhibit the most significant stress on the internal-side of the masonry walls. The continuous deformation of plaster materials stems from the cumulative effects of various factors such as rain, moisture, seismic activity, wind, and thermal conditions, contributing to the structural deterioration and damage observed in these towers.

The analysis included evaluating stress and deformation capabilities at various locations within the four towers, as depicted in Fig. 13. Stress responses exhibited approximate similarity across the towers during dead and live loads (Fig. 14). Stress behaviour (Fig. 14a) appeared concurrently due to substantial ground and first-floor massiveness, with minor variations observed on the upper-floors of CT&FCT. SST&BCT displayed comparable stress responses. Regarding deformation, CT&FCT exhibited significant differences, while SST&BCT showed akin responses (Fig. 14b).

CT, constructed entirely with brick masonry load-bearing walls, exhibited notably higher stress responses than other towers. While stress responses were generally consistent throughout the tower due to comprehensive connectivity up to the second-floor, substantial deformation responses were noted during analysis. SST, independently designed from three directions from the ground-floor to the dome, manifested substantial stress and deformation, particularly witnessing significant internal structural losses. FCT, a blend of stone and masonry construction, displayed varied stress and deformation responses owing to its connection on two sides of the building. The tower's stress and deformation responses during analysis concurred with those visible during visual-inspections. BCT, fully simulated in brick masonry but with an upper portion in stone materials,

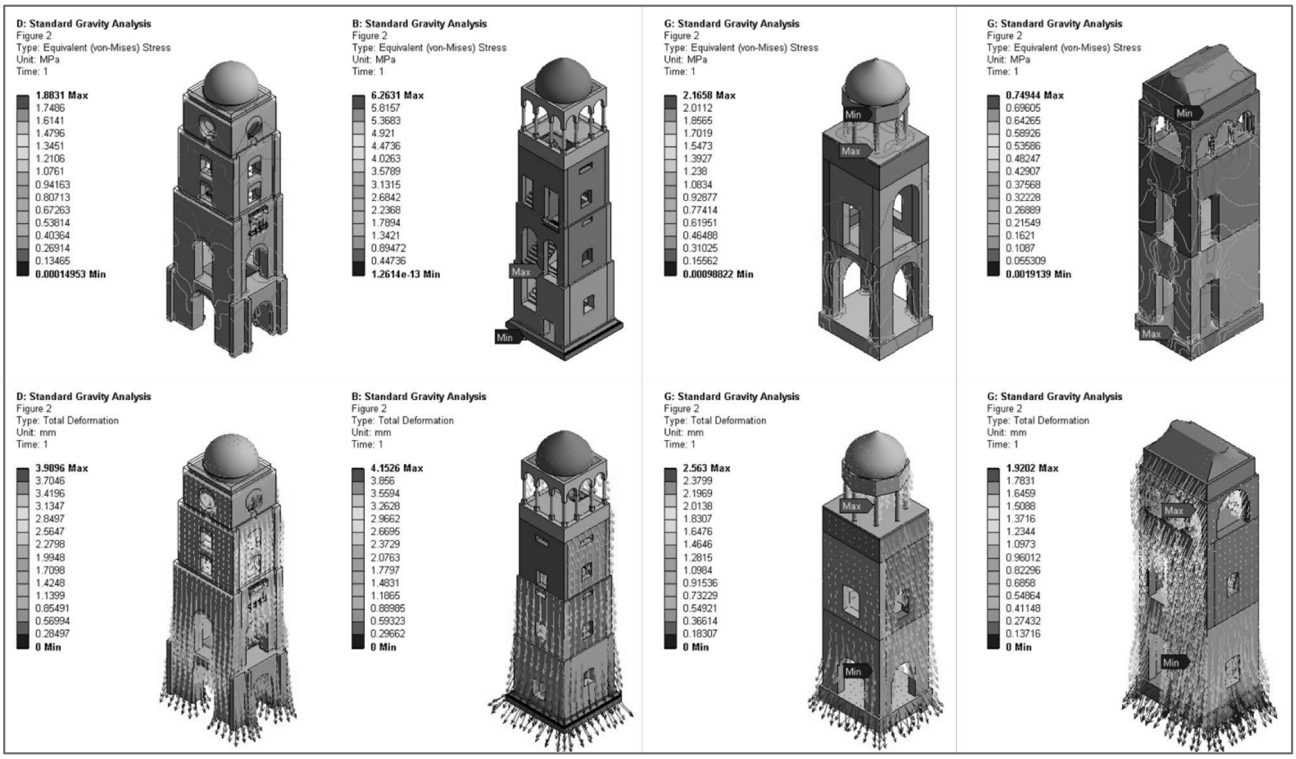

(a) Stress and deformation response under gravity loading

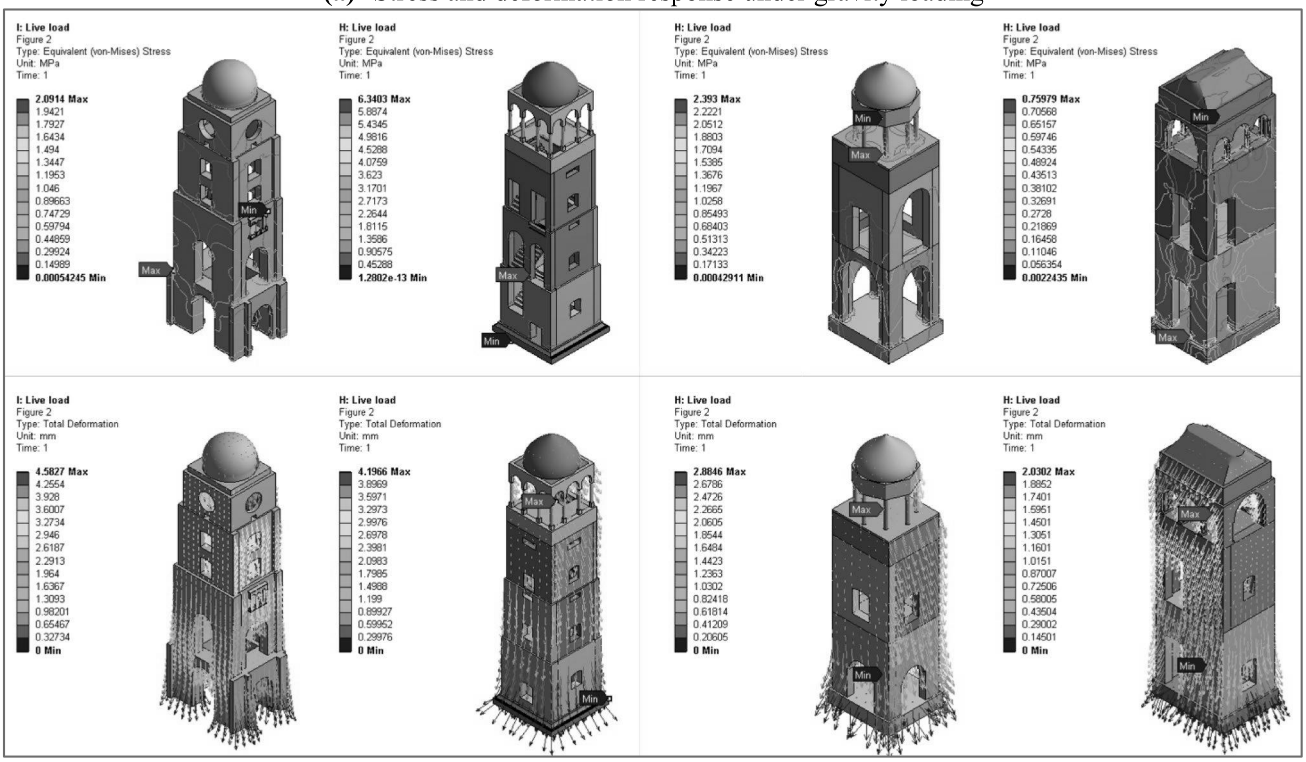

(b) Stress and deformation response under live loading

Fig. 13 Responses during static loading of towers

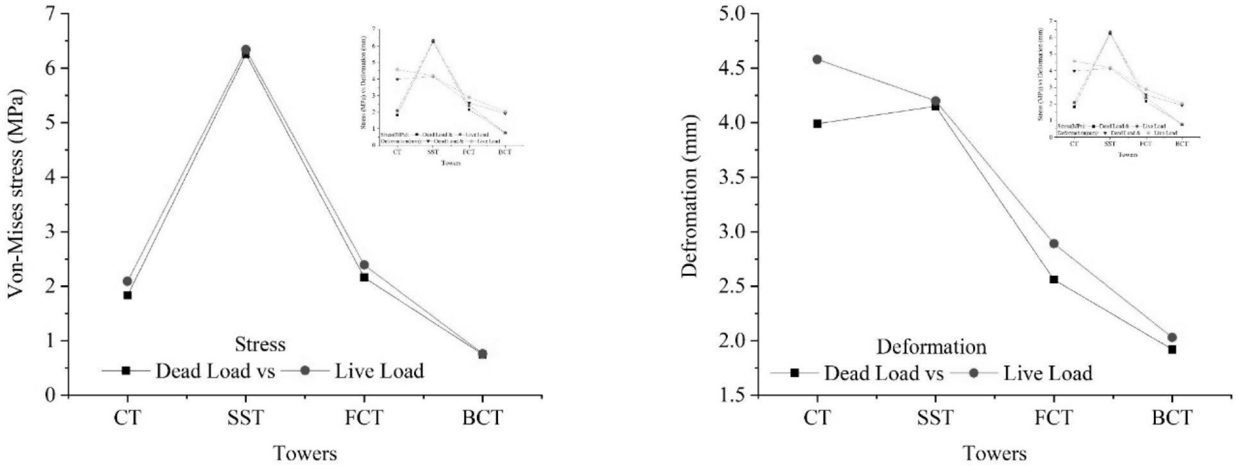

(a) Stress comparison of Dead load vs Live load of four towers

(b) Deformation comparison of Dead load vs Live load of four towers

Fig. 14 Stress and deformation comparision of towers

experienced stress responses closely tied to deformation. Significant deformation was observed compared to stress responses, reflecting major cracks evident during tower inspections.

Modal Analysis

Conducted through a 3D-FE model utilizing linear elastic materials, dynamic modal analysis assessed tower behaviour. This evaluation encompassed similar material properties and boundary conditions for all towers. The study entailed free-vibration modal analysis to determine natural frequencies and six-mode shapes per tower [9, 11, 22, 43]. Discussions with the responsible engineer confirmed the tower's independent construction, notably separate from the SH structure. This prompts an exploration of whether the strength increment adequately safety amidst elevated stress. A comprehensive free vibration modal analysis of the entire tower is executed to investigate further, adhering to established mechanical methods. This will involve appropriate masses and elastic stiffness of the structural system, yielding natural periods (T) and mode shapes {Φ} for its various vibration modes.

$$[K]\{\varnothing_i\} = w_i^2[M]\{\varnothing_i\} \tag{14}$$

$[K]$= stiffness matrix;$\{\varnothing_i\}$= mode shape vector (eigenvector) of mode i;w^i= natural circular frequency of mode i (w_i^2 is the eigenvalue);$[M]$= mass matrix.

Following non-destructive testing, the towers underwent detailed numerical analysis to evaluate their dynamic mechanical properties. The results revealed the first six mode shapes, as illustrated in Fig. 15. These modes provide insights into how each tower responds to dynamic loading. For the Central Tower (CT), the first six natural frequencies were recorded as 1.68, 2.09, 3.85, 5.54, 6.33, and 8.47 Hz. The first and second modes showed deformations in the longitudinal and transverse directions, respectively, while the third mode indicated torsional behavior. These early modes suggest that as the tower becomes more geometrically flexible, the vibration periods increase. The deformation amplitudes in the first and second modes were 4.41 mm and 4.72 mm, respectively. In the case of the Side Stair Tower (SST), the first and sixth mode frequencies were 2.26 Hz and 7.56 Hz. The six identified modal frequencies for SST were 2.26, 2.37, 4.33, 4.79, 4.95, and 7.56 Hz. The first mode displayed deformation in the X-direction (longitudinal), the second mode in the Z-direction (transverse), and the third mode showed a triangular deformation pattern, similar to that of the CT. The Front Corner Tower (FCT), which features stone on the ground floor and thick masonry on the first floor, exhibited the first three modal frequencies as 2.29 Hz, 2.58 Hz, and 3.94 Hz. The modal behavior of FCT closely matched that of CT and SST, reflecting the influence of massive construction techniques. In the Back Corner Tower (BCT), significant responses were observed in both longitudinal and transverse directions. The first two natural frequencies were 2.44 Hz and 3.07 Hz, while the third mode, occurring at 6.04 Hz, represented torsional behavior. The use of brick masonry, similar to that in CT, influenced BCT's modal characteristics..

Time History Analysis

The building's tower construction employed an unreinforced massive approach with specific materials. Dynamic

Fig. 15 Mode-shape of tower element

time history responses were examined at each SH-building tower level. A meticulous visual-inspection guided location choices for evaluation despite challenges posed by cracks and damages. A lumped-mass model evaluated longitudinal direction response across all towers and floors [5, 9, 10, 22, 28, 36, 39]. The building features substantial mass and interconnecting dimensions, exhibiting more transverse than longitudinal responsiveness.

The masonry CT structure's response has been assessed across its levels, from the ground-floor to the dome. The response characteristics of each floor are illustrated in Fig. 16. Notably, the acceleration response varies across the structure, registering a minimum of 2.398 mm/s^2 on the ground-floor and peaking at 25.696 mm/s^2 at the dome. Throughout the structure, the response is predominantly oriented in the negative direction, except on the fourth floor, where a positive response of 20.695 mm/s^2 is observed. The entire response pattern of the CT maintains a consistent time duration of approximately 68 s shown in Fig. 16a. The evaluation of longitudinal deformation response within the CT structure, depicted in Fig. 16b, reveals minor variations across each level. The smallest and largest responses are observed on the ground-floor and the dome, measuring 0.039 mm and 0.43 mm, respectively. The overall deformation pattern within the masonry tower exhibits a progression from negative values on the ground-floor to the dome. The dynamic response is only minimally affected, attributed to the substantial foundation and the symmetrical brick

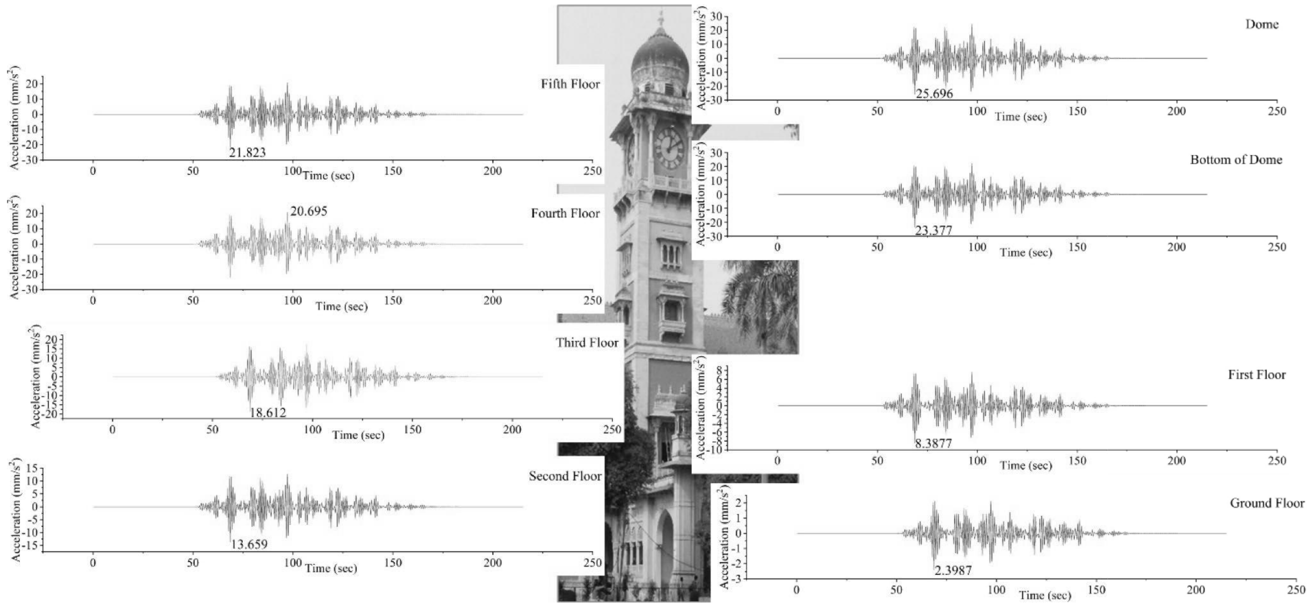

(a) Acceleration response

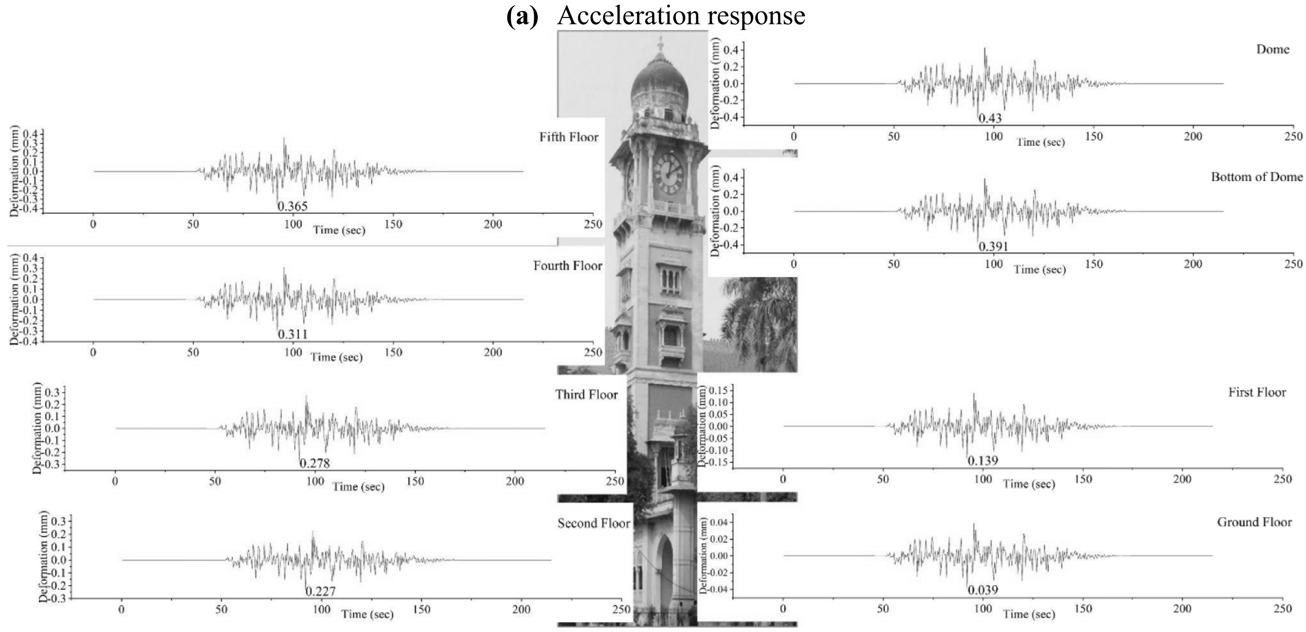

(b) Deformation response

Fig. 16 Clock tower responses

masonry wall of the CT. As the tower's height decreases due to diminishing wall thickness, the responses gradually increase in tandem. Notably, the second-floor level presents the most pronounced responses, particularly in connection areas and openings within the tower.

The stress distribution within the CT structure has been assessed for its dynamic behaviour, encompassing the spatial transition from the ground-floor to the dome, as illustrated in Fig. 16c. At the junction of the masonry wall and the roof on the ground-floor, the maximum stress response measures 0.169 MPa. Likewise, at a fixed-thickness plinth 1.07 m above the ground, the stress response registers at 0.123 MPa. As one ascends from the first-floor to the fifth-floor of the CT, the stress response decreases in a gradient, ranging from 0.119 MPa to 8.485×10^{-4} MPa. In the context of the dome section of the CT, stress distribution manifests as 0.00162 MPa at the lower dome-masonry connection and 1.333×10^{-4} MPa on the upper dome surface. Multiple stress concentration points have been identified throughout the structural heights, including the ground floor to the fifth floor. These include masonry walls, arches, columns, roofs, dome elements, and various connections such

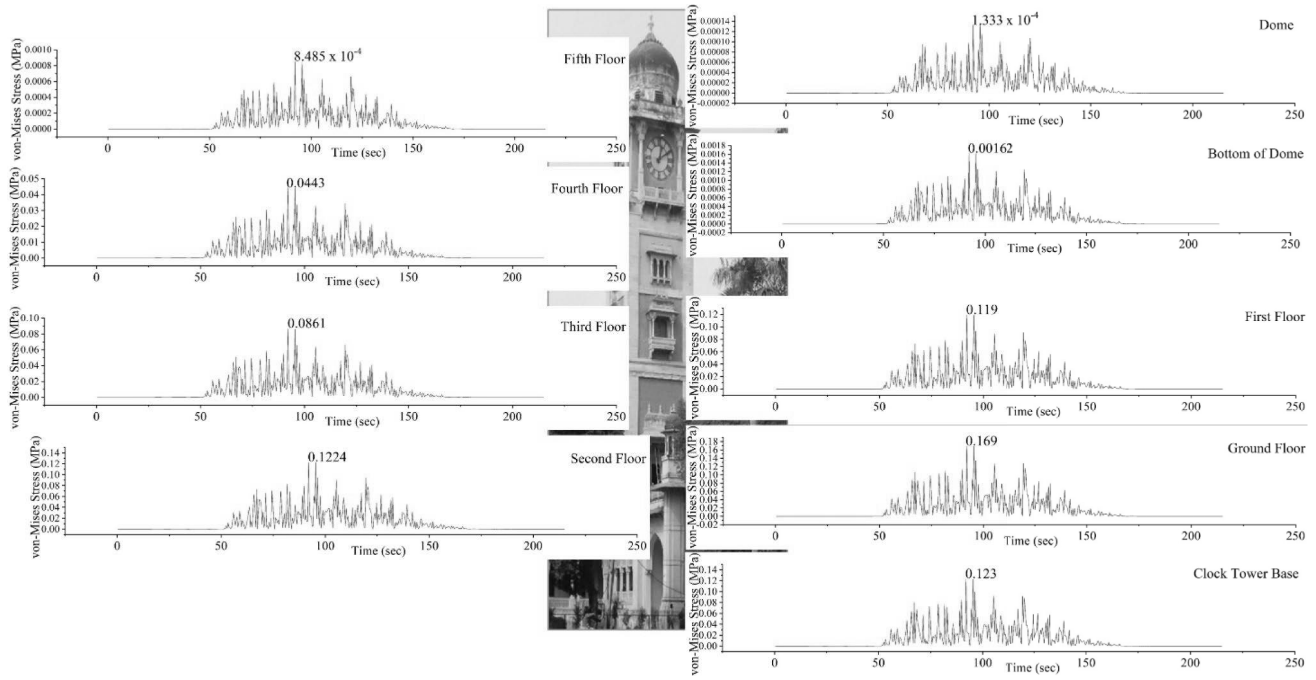

(c) Stress response

Fig. 16 (continued)

as wall-to-wall, wall-to-roof, arch-to-arch, and arch-to-wall interfaces. Openings such as doors, windows, ventilators, and arch-crowns exhibit stress variations. Prevalently, the most significant stress concentrations arise within the entire tower's masonry walls and arch components. These high-stress areas correlate with observable cracks and structural impairments, which were discernible during on-site tower surveys.

The Side Stair Tower (SST) is the second-tallest tower in the SH building. A time-history analysis was conducted to evaluate its dynamic response, focusing on acceleration, deformation, and stress. The acceleration response is shown in Fig. 17, where the highest acceleration, 198.12 mm/s^2, occurs at the top of the dome. The lowest value, 2.39 mm/s^2, is recorded at the ground floor. The trend shows increasing acceleration with height, similar to the Central Tower (CT). Higher acceleration values are concentrated at the stone elements, particularly panels, and drums. At the first and third floors, acceleration ranges from 15.14 mm/s^2 to 75.65 mm/s^2 (Fig. 17a), reflecting the SST's mixed construction—brick masonry and stone. Thick masonry walls and arches dominate from the ground to second floor, while the third floor features stone arches and panels. Figure 17b shows the deformation response, which also increases with height. The maximum deformation of 4.74 mm occurs at the dome, while the minimum, 0.41 mm, is observed at the first-floor roof. Negligible deformation was found at ground level. Stone elements recorded 2.24 mm in arches and 3.26 mm in drums. Brick masonry showed minimal deformation due to its mass. The stress response is detailed in Fig. 17c. The maximum stress, 0.125 MPa, is recorded at the tower base, and 0.021 MPa at the stair-masonry wall junction on the second floor. Minor stresses were noted at stone arches, arch crowns, and window crowns. Inside the dome, stress was negligible at ~ 10^{-5} MPa, confirming limited internal load transfer.

The FCT is the third-tallest tower in the SH building complex and differs from CT and SST in its construction. It integrates stone arches and brick masonry, with office space on the first floor, and stone vaults on the ground and second floors supporting a dome. The tower's dynamic behaviour under seismic loading was evaluated through time-history analysis. As shown in Fig. 18, the acceleration response increases with height, peaking at 190.96 mm/s^2 at the dome's apex and reaching a minimum of 0.188 mm/s^2 at the strong 1.07 m-thick plinth base. Intermediate floor responses range from 34.06 mm/s^2 to 178.77 mm/s^2 (Fig. 18a). Stone vaults on the ground floor and a drum-column-dome system on the third floor largely influence this response.

The deformation response (Fig. 18b) follows a similar trend, increasing with elevation. The dome registers the highest deformation of 4.356 mm, while the base exhibits a negligible 0.0049 mm. Floor-wise deformations range between 0.966 mm and 4.066 mm. Cracks and structural issues were particularly noticeable at arches, columns, and walls of the ground and third floors, confirmed through

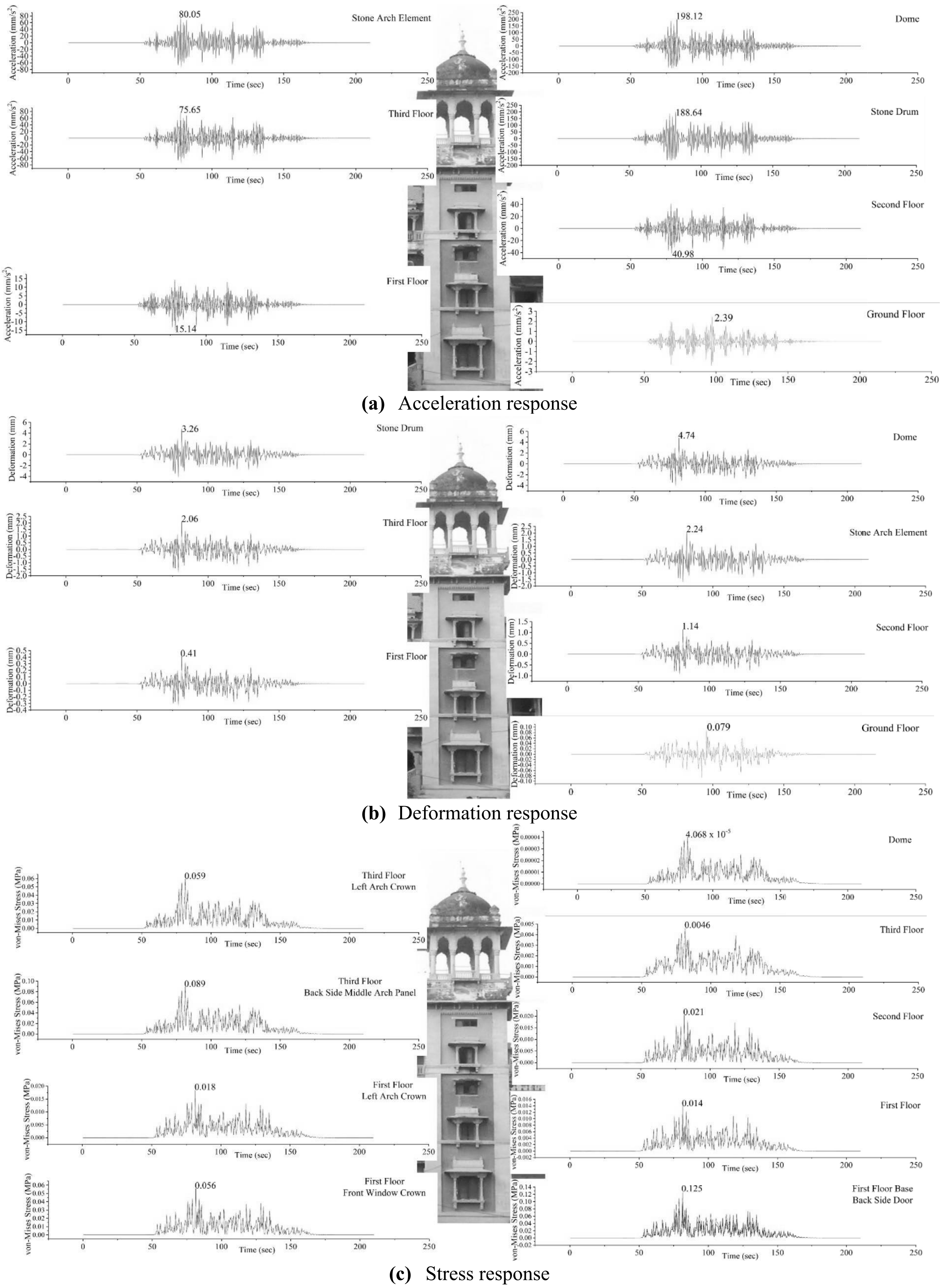

Fig. 17 Side stair tower responses

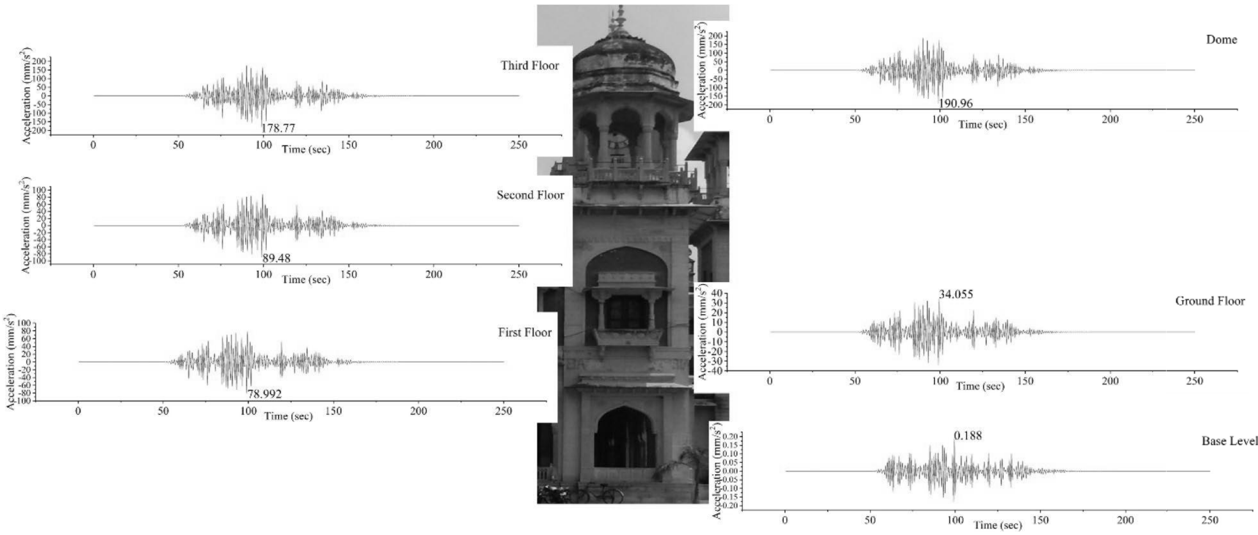

(a) Acceleration response

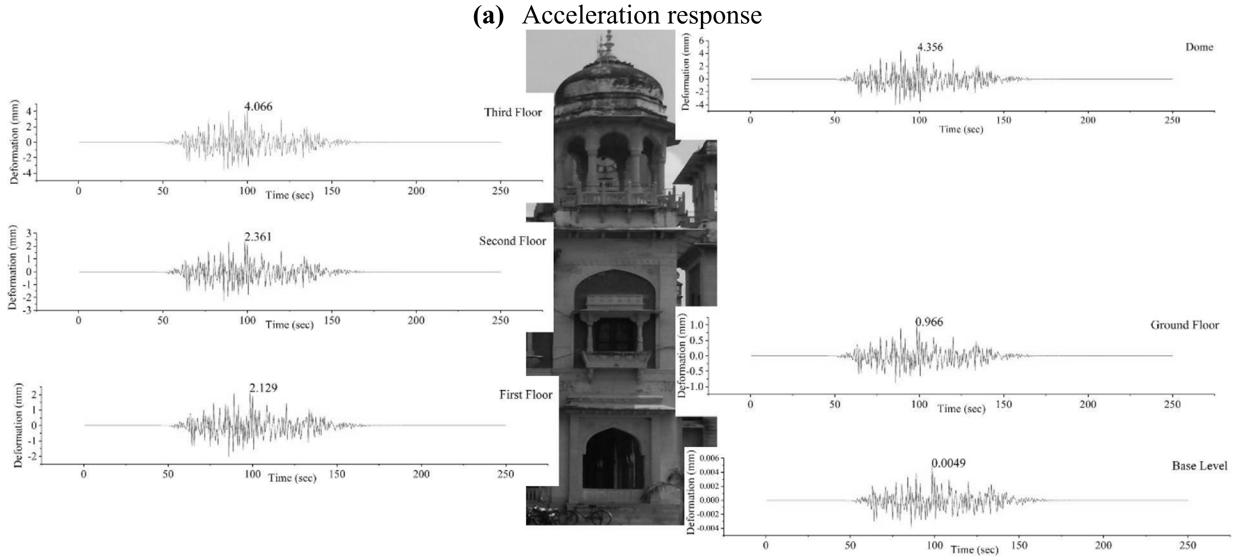

(b) Deformation response

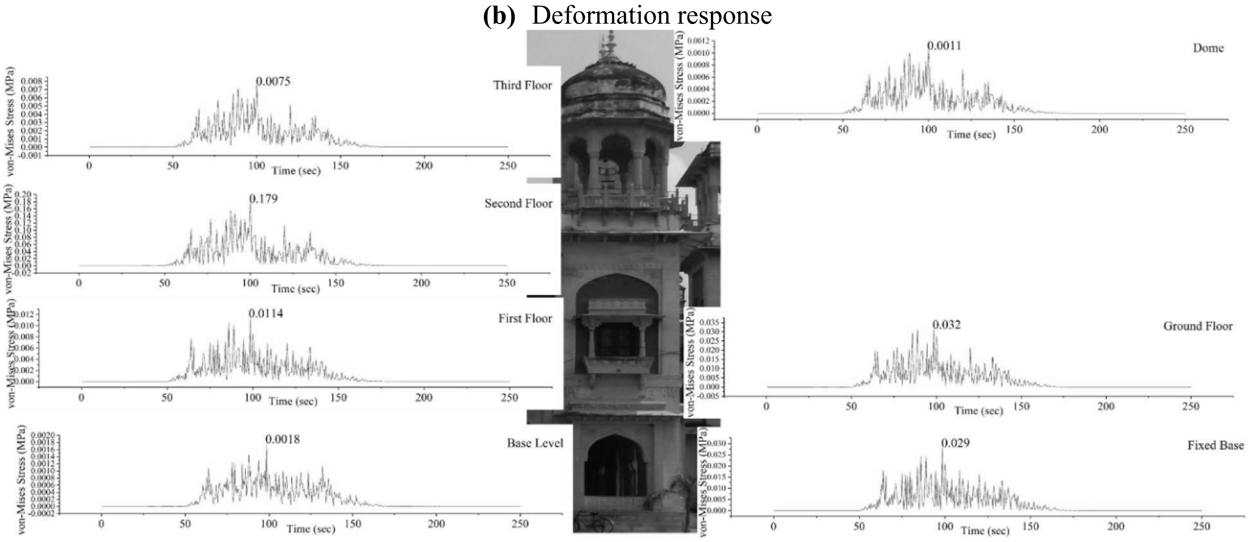

(c) Stress response

Fig. 18 Front corner tower responses

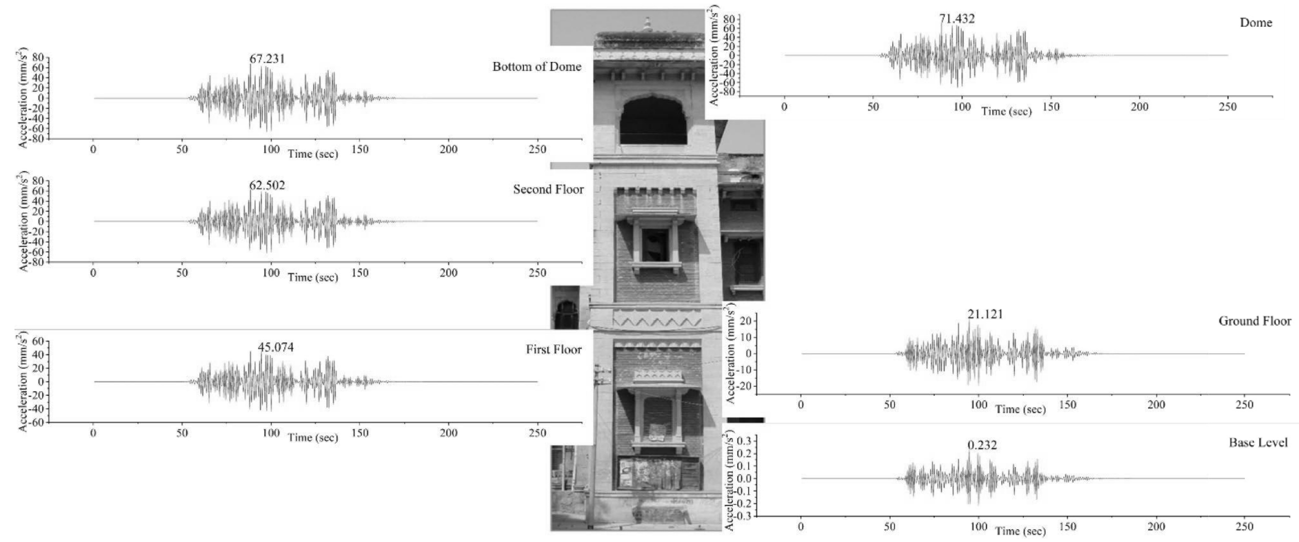

(a) Acceleration response

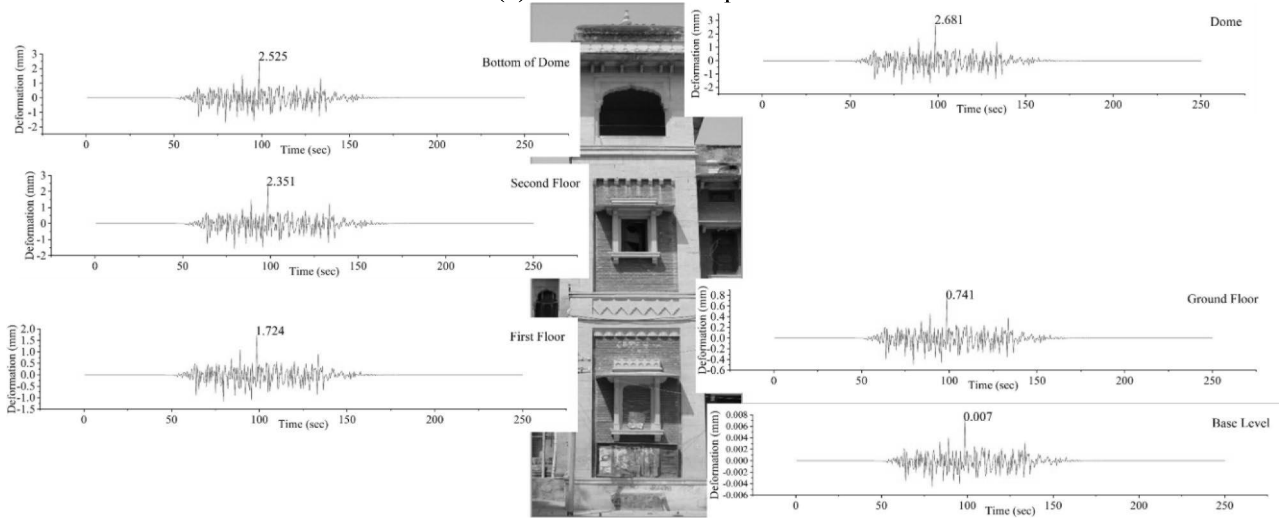

(b) Deformation response

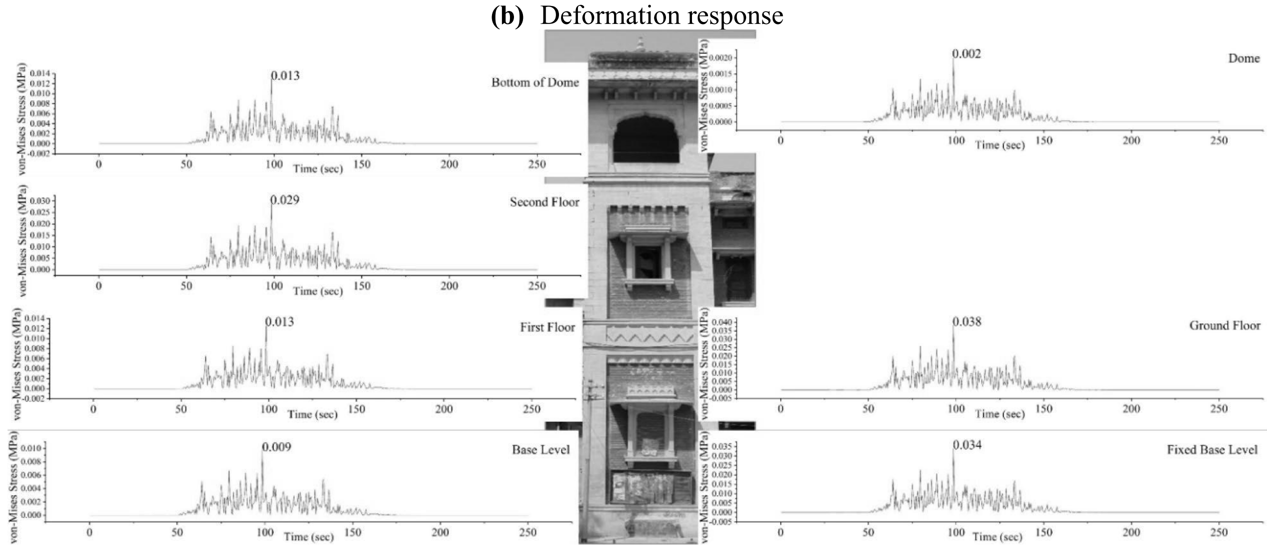

(c) Stress response

Fig. 19 Back corner tower responses

Table 9 Comparison of static and dynamic responses of four-tower

Static analysis								
Towers	Dead load				Live load			
	CT	SST	FCT	BCT	CT	SST	FCT	BCT
Stress (MPa)	1.88	6.26	2.17	0.75	2.09	6.34	2.39	0.76
Deformation (mm)	3.99	4.15	2.56	1.92	4.58	4.19	2.88	2.03

Dynamic Analysis

Towers	Natural frequencies (Hz)					
	Mode-1	Mode-2	Mode-3	Mode-4	Mode-5	Mode-6
CT	1.68	2.09	3.85	5.54	6.33	8.47
SST	2.27	2.37	4.33	4.79	4.96	7.56
FCT	2.29	2.59	3.94	4.49	4.52	6.33
BCT	2.45	3.07	6.05	8.29	10.07	13.95

Ground motion responses in Towers

Responses	Acceleration (mm/s^2)				Deformation (mm)				Stress (MPa)			
Locations	CT	SST	FCT	BCT	CT	SST	FCT	BCT	CT	SST	FCT	BCT
Fixed Base	**	**	**	**	**	**	**	**	**	**	0.029	0.034
Base Level	**	**	0.188	0.232	**	**	0.0049	0.007	0.123	0.125	0.0018	0.009
Ground Floor	2.39	2.39	34.055	21.121	0.039	0.079	0.966	0.741	0.169	**	0.032	0.038
First Floor	8.38	15.14	78.992	45.074	0.139	0.41	2.129	1.724	0.119	0.014	0.0114	0.013
Second Floor	13.66	40.98	89.48	62.502	0.227	1.14	2.361	2.351	0.122	0.021	0.179	0.029
Third Floor	18.61	75.65	178.77	**	0.278	2.06	4.066	**	0.086	0.005	0.0075	**
Fourth Floor	20.69	**	**	**	0.311	**	**	**	0.044	**	**	**
Fifth Floor	21.82	**	**	**	0.365	**	**	**	8.48×10^{-4}	**	**	**
Bottom of Dome	23.38	188.64	**	67.231	0.391	3.26	**	2.525	0.002	0.089	**	0.013
Dome	25.69	198.12	190.96	71.432	0.43	4.74	4.356	2.681	1.33×10^{-4}	4.068×10^{-5}	0.0011	0.002

**Location not identified during the visual-inspection on-site inspections. As illustrated in Fig. 18c, the stress distribution varies across the height. The maximum stress, 0.179 MPa, occurs at the roof-wall connection on the second floor, while the lowest, 0.0011 MPa, is observed at the first-floor roof and dome column junctions. These stress zones correspond to observed damage points, indicating structural vulnerability at these connections.

The BCT, located at the rear of the SH building, is the fourth-tallest tower in the complex. Its structure consists of brick masonry walls on the ground and first floors, with stone arches and panels on all sides of the second floor. The tower's acceleration response is illustrated in Fig. 19a, where the highest acceleration of 71.432 mm/s^2 occurs at the dome apex, and the lowest of 0.232 mm/s^2 is at the plinth. Acceleration increases steadily with height and closely mirrors trends seen in CT, SST, and FCT towers. The tower's deformation behaviour is shown in Fig. 19b. Deformation increases with height, starting from 0.007 mm at the plinth, rising to 0.741 mm on the ground floor, 1.724 mm on the first floor, and 2.351 mm on the second floor. At the dome, deformations reach 2.525 mm at the base and 2.681 mm at the top. Stress responses are presented in Fig. 19c, with the highest stress of 0.038 MPa found at the ground-floor masonry wall junction. Other notable stress points include 0.034 MPa at the tower's fixed base and 0.009 MPa at the plinth (1.07 m thick). Dome stresses range from 0.013 MPa near the base to 0.002 MPa at the top. Compared to other towers, BCT shows lower stress levels due to strong masonry design on the lower floors.

Comparison of Tower Responses

Static and dynamic analyses of the four towers revealed that the SST tower experienced the highest stress and deformation under dead-load conditions. This can be attributed to its structural configuration—unlike the other towers, which are connected to the main building on two sides, the SST is only connected on one side up to the first floor. Under live-load conditions, SST again showed maximum stress, while the CT tower's dome recorded the greatest deformation.

In the modal analysis, the BCT tower exhibited the highest natural frequencies among all towers. The first six modes of the towers demonstrated comparable frequency ranges, as outlined in Table 9. While the first three towers peaked in the sixth mode, BCT showed similar peak frequencies between the third and fourth modes.

Ground-motion analysis recorded acceleration, deformation, and stress responses at key floor levels for each tower, also summarized in Table 9. Visual inspection confirmed that the upper levels, particularly those composed of stonework and domes, were the most responsive. The unreinforced masonry walls showed notable responses, whereas structural connections exhibited minimal activity. The masonry façades mainly remained unaffected.

However, visible damage was observed in the walls and connection zones across all towers, mainly due to the loss of binding material at each floor. In particular, the roof and dome binding materials suffered internal collapse, leading to large cracks on both sides of the roof elements.

Conclusions

This comprehensive numerical investigation assessed the structural performance of the masonry towers in the historic SH building at Allahabad University, India, using non-destructive testing (NDT) and finite element simulations. The modelling integrated data from archival records, site surveys, and photographic documentation, ensuring realistic geometry and material properties. On-site observations indicated the towers are generally stable, though minor cracks were found around doorways, windows, and staircases. Overall, the brick and stonework demonstrated notable resilience.

However, serious concerns emerged on the upper floors, where material deterioration and partial collapses have restricted access. Loss of binding materials and construction joints compromised the integrity of structural interconnections. Unplastered upper sections showed significant damage from environmental exposure.

Using macro modelling, both static and dynamic responses were analysed across the four towers. The SST tower displayed the highest stresses under dead and live load (see Fig. 3, Table 9), while the CT dome showed maximum deformation. The BCT tower recorded the highest natural frequencies, with detailed comparisons in Table 9. Time history analysis with synthetic ground motion revealed peak acceleration, stress, and deformation at upper levels, especially near domes and stairs.

This study confirms that the ground and first floors of the towers remain in good structural condition, while the upper levels require urgent intervention. Preservation efforts should focus on strengthening staircases, connections, and binding joints in the upper portions to maintain the structural integrity and heritage value of these Indo-Saracenic-style masonry towers.

Declarations

Conflict of Interest On behalf of all authors, the corresponding author states that there is no conflict of interest.

Replication of results The results presented in the research are performed on FEM tools using standard methods. Hence, one can perform the replication using the method given above.

References

1. P. Roca, The study and restoration of historical structures: From principles to practice, Struct. Anal. Hist. Constr. (2006) 9–24.
2. S. Burman, K. Pallav, K.D. Singh, Finite element modelling of 'Rang Ghar'monument, Assam. Int. J. Innov. Res. Sci. Eng. Technol. **3**, 144–151 (2014)
3. L.F. Ramos, F. Casarin, C. Algeri, P.B. Lourenço, C. Modena, Investigation techniques carried out on the Qutb Minar, New, in: Test, 2006: pp. 1–8.
4. R.N. Dubey, Shashi K. Thakkar, A. Gupta, Seismic Analysis for Safety Evaluation of Taj Mahal Monument, Elev. World Conf. Earthq. Eng. (1996).
5. A. Anzani, L. Binda, A. Carpinteri, S. Invernizzi, G. Lacidogna, A multilevel approach for the damage assessment of historic masonry towers. J. Cult. Herit. **11**, 459–470 (2010). https://doi.org/10.1016/j.culher.2009.11.008
6. A. Bayraktar, A. Şahin, D.M. Özcan, F. Yildirim, Numerical damage assessment of Haghia Sophia bell tower by nonlinear FE modeling. Appl. Math. Model. **34**, 92–121 (2010). https://doi.org/10.1016/j.apm.2009.03.033
7. L. Binda, L. Zanzi, M. Lualdi, P. Condoleo, The use of georadar to assess damage to a masonry Bell Tower in Cremona, Italy. NDT E Int. **38**, 171–179 (2005). https://doi.org/10.1016/j.ndteint.2004.03.010
8. A. Carpinteri, S. Invernizzi, G. Lacidogna, In situ damage assessment and nonlinear modelling of a historical masonry tower. Eng. Struct. **27**, 387–395 (2005). https://doi.org/10.1016/j.engstruct.2004.11.001
9. M. Acito, M. Bocciarelli, C. Chesi, G. Milani, Collapse of the clock tower in Finale Emilia after the May 2012 Emilia Romagna earthquake sequence: numerical insight. Eng. Struct. **72**, 70–91 (2014). https://doi.org/10.1016/j.engstruct.2014.04.026

10 G. Camata, L. Cifelli, E. Spacone, J. Conte, M. Loi, P. Torrese, Seismic safety assessment of the tower of the S. Maria Maggiore Cathedral in Guardiagrele, Italy. Civil-Comp Proc. (2008). https://doi.org/10.4203/ccp.88.58

11. S. Casolo, G. Milani, G. Uva, C. Alessandri, Comparative seismic vulnerability analysis on ten masonry towers in the coastal Po Valley in Italy. Eng. Struct. **49**, 465–490 (2013). https://doi.org/10.1016/j.engstruct.2012.11.033
12. K. Bernardeschi, C. Padovani, G. Pasquinelli, Numerical modelling of the structural behaviour of Buti's bell tower. J. Cult. Herit. **5**, 371–378 (2004). https://doi.org/10.1016/j.culher.2004.01.004
13. F. Ceroni, M. Pecce, F. Palmaccio, G. Manfredi, Structural investigations and modelling of the Bell Tower of Santa Maria del Carmine. WIT Trans. Built Environ. **95**, 655–666 (2007). https://doi.org/10.2495/STR070611

14 M. Girardi, C. Padovani, A. Pagni, G. Pasquinelli, Numerical modelling of masonry towers: The case study of the "Rognosa" tower in San Gimignano. Adv. Trends Struct. Eng. Mech. Comput. Proc. 4th Int Conf. Struct. Eng. Mech. Comput. SEMC **2010**, 993–996 (2010)

15. M.L. Beconcini, S. Bennati, W. Salvatore, Structural characterisation of a medieval bell tower: First historical, experimental and numerical investigations, Proc., 3rd Int. Semin. Struct. Anal. Hist. Constr. Hist. Constr. 2001, Possibilities Numer. Exp. Tech. (2001) 431–444.
16. O. Bergamo, G. Campione, G. Russo, E. Motta, Testing of "Global Young's Modulus E" on a rehabilitated masonry bell tower in Venice. Eng. Fail. Anal. **78**, 15–28 (2017). https://doi.org/10.1016/j.engfailanal.2017.02.017
17. C. Alessandri, V. Mallardo, Structural assessments of the Church of the Nativity in Bethlehem. J. Cult. Herit. **13**, e61–e69 (2012). https://doi.org/10.1016/j.culher.2012.10.010
18. V. Arcidiacono, G.P. Cimellaro, J.A. Ochsendorf, Analysis of the failure mechanisms of the basilica of Santa Maria di Collemaggio during 2009 L'Aquila earthquake. Eng. Struct. **99**, 502–516 (2015). https://doi.org/10.1016/j.engstruct.2015.04.051

19 A. Orduña, A. Preciado, F. Galván, J.C. Araiza, Vulnerability assessment of churches at Colima by 3D limit analysis models. Struct. Anal. Hist. Constr. Preserv. Saf. Significance Proc. 6th Int Conf. Struct. Anal. Hist. Constr. SAHC08 **2**, 1297–1302 (2008). https://doi.org/10.1201/9781439828229.ch149

20. R.N. Misra, Architectural Triveni of Allahabad and Asphyxiation of a Monumental Dream: (P.K. Acharya and His Manasara). Humanit. Soc. Sci. (2016) 10.
21. M. Valente, G. Milani, Seismic assessment of historical masonry towers by means of simplified approaches and standard FEM. Constr. Build. Mater. **108**, 74–104 (2016). https://doi.org/10.1016/j.conbuildmat.2016.01.025
22. M. Valente, G. Milani, Non-linear dynamic and static analyses on eight historical masonry towers in the North-East of Italy. Eng. Struct. **114**, 241–270 (2016). https://doi.org/10.1016/j.engstruct.2016.02.004
23. A. Kaveh, M. Maniat, Damage detection based on MCSS and PSO using modal data. Smart Struct. Syst. **15**, 1253–1270 (2015)
24. C. Gentile, A. Saisi, Ambient vibration testing of historic masonry towers for structural identification and damage assessment. Constr. Build. Mater. **21**, 1311–1321 (2007). https://doi.org/10.1016/j.conbuildmat.2006.01.007
25. G. Russo, O. Bergamo, L. Damiani, D. Lugato, Experimental analysis of the "Saint Andrea" Masonry Bell Tower in Venice. A new method for the determination of "Tower Global Young's Modulus E." Eng. Struct. **32**, 353–360 (2010). https://doi.org/10.1016/j.engstruct.2009.08.002
26. G. Bartoli, M. Betti, S. Giordano, In situ static and dynamic investigations on the " Torre Grossa" masonry tower. Eng. Struct. **52**, 718–733 (2013). https://doi.org/10.1016/j.engstruct.2013.01.030
27. D. Colapietro, A. Fiore, A. Netti, F. Fatiguso, G.C. Marano, M. De Fino, D. Cascella, A. Ancona, Dynamic identification and evaluation of the seismic safety of a masonry bell tower in the south of Italy, ECCOMAS Themat. Conf. - COMPDYN 2013 4th Int. Conf. Comput. Methods Struct. Dyn. Earthq. Eng. Proc. - An IACM Spec. Interes. Conf. (2013) 3459–3470. https://doi.org/10.7712/120113.4751.c1418
28. S. Ivorra, F.J. Pallarés, Dynamic investigations on a masonry bell tower. Eng. Struct. **28**, 660–667 (2006). https://doi.org/10.1016/j.engstruct.2005.09.019
29. M. Pieraccini, D. Dei, M. Betti, G. Bartoli, G. Tucci, N. Guardini, Dynamic identification of historic masonry towers through an expeditious and no-contact approach: Application to the "Torre del Mangia" in Siena (Italy). J. Cult. Herit. **15**, 275–282 (2014). https://doi.org/10.1016/j.culher.2013.07.006
30. H. Qin, X. Zhao, Y. Chen, B. Wang, Title: Elasto-Plastic Time-History Analysis of the Shanghai Tower Under Rare Earthquakes Elasto-plastic time-history analysis of the Shanghai Tower under rare earthquakes, (2011).
31. G. Milani, S. Casolo, A. Naliato, A. Tralli, Seismic assessment of a medieval masonry tower in Northern Italy by limit, nonlinear static, and full dynamic analyses. Int. J. Archit. Herit. **6**, 489–524 (2012). https://doi.org/10.1080/15583058.2011.588987

32 A. Kaveh, *Optimal Analysis of Structures by Concepts of Symmetry and Regularity* (Springer Verlag, Berlin, 2013). https://doi.org/10.1007/978-3-7091-1565-7

33. G. Barbieri, M. Valente, L. Biolzi, C. Togliani, L. Fregonese, G. Stanga, An insight in the late Baroque architecture: an integrated approach for a unique Bibiena church. J. Cult. Herit. **23**, 58–67 (2017). https://doi.org/10.1016/j.culher.2016.07.006
34. G. Milani, S. Russo, M. Pizzolato, A. Tralli, Seismic behavior of the San Pietro di Coppito Church bell tower in L'Aquila, Italy.

Open Civ. Eng. J. **6**, 131–147 (2012). https://doi.org/10.2174/1874149501206010131
35. F. Peña, P.B. Lourenço, N. Mendes, D.V. Oliveira, Numerical models for the seismic assessment of an old masonry tower. Eng. Struct. **32**, 1466–1478 (2010). https://doi.org/10.1016/j.engstruct.2010.01.027
36. A. Preciado, Seismic vulnerability and failure modes simulation of ancient masonry towers by validated virtual finite element models. Eng. Fail. Anal. **57**, 72–87 (2015). https://doi.org/10.1016/j.engfailanal.2015.07.030p
37. P. Riva, F. Perotti, E. Guidoboni, E. Boschi, Seismic analysis of the Asinelli Tower and earthquakes in Bologna. Soil Dyn. Earthquake Eng. **17**, 525–550 (1998). https://doi.org/10.1016/S0267-7261(98)00009-8
38. L. Salvatori, A.M. Marra, G. Bartoli, P. Spinelli, Probabilistic seismic performance of masonry towers : General procedure and a simplified implementation. Eng. Struct. **94**, 82–95 (2015). https://doi.org/10.1016/j.engstruct.2015.02.017
39. A. Saisi, C. Gentile, M. Guidobaldi, Post-earthquake continuous dynamic monitoring of the Gabbia Tower in Mantua, Italy. Constr. Build. Mater. **81**, 101–112 (2015). https://doi.org/10.1016/j.conbuildmat.2015.02.010
40. A. Saisi, C. Gentile, Post-earthquake diagnostic investigation of a historic masonry tower. J. Cult. Herit. **16**, 602–609 (2015). https://doi.org/10.1016/j.culher.2014.09.002
41. M. Acito, C. Chesi, G. Milani, S. Torri, Collapse analysis of the Clock and Fortified towers of Finale Emilia, Italy, after the 2012 Emilia Romagna seismic sequence: lesson learned and reconstruction hypotheses. Constr. Build. Mater. **115**, 193–213 (2016). https://doi.org/10.1016/j.conbuildmat.2016.03.220
42. M. Acito, M. Buzzetti, C. Chesi, E. Magrinelli, G. Milani, Failures and damages of historical masonry structures induced by 2012 northern and 2016–17 central Italy seismic sequences: critical issues and new perspectives towards seismic prevention. Eng. Fail. Anal. **149**, 107257 (2023). https://doi.org/10.1016/j.engfailanal.2023.107257
43. T. Choudhury, G. Milani, M. Acito, C. Chesi, D. Francesco, I. Carabellese, G. Martines, V. De Simone, Damage Survey and Structural Assessment of the Rosario Church in Finale Emilia After the May 2012 Earthquake in Emilia-Romagna , Italy, Proc. 9th Int. Conf. Struct. Anal. Hist. Constr. SAHC 2014. (2014) 14–17.
44. P. Pineda, Collapse and upgrading mechanisms associated to the structural materials of a deteriorated masonry tower. Nonlinear assessment under different damage and loading levels. Eng. Fail. Anal. **63**, 72–93 (2016). https://doi.org/10.1016/j.engfailanal.2016.02.013
45. G. Penelis, G. Penelis, Restoration of the Margirgis Church and Roman Tower in Cairo. Struct. Eng. Int. **30**, 64–73 (2020). https://doi.org/10.1080/10168664.2019.1625738
46. A. Preciado, G. Bartoli, A. Ramírez-Gaytán, Earthquake protection of the Torre Grossa medieval tower of San Gimignano, Italy by vertical external prestressing. Eng. Fail. Anal. **71**, 31–42 (2017). https://doi.org/10.1016/j.engfailanal.2016.11.005
47. A. Aşıkoğlu, J.D. Anna, R. Ramirez, F. Solarino, Simulation of blind pre - diction and post - diction shaking table tests on a masonry building aggregate using a continuum modelling approach, Springer. Netherlands (2023). https://doi.org/10.1007/s10518-023-01666-2
48. F. Solarino, D.V. Oliveira, L. Giresini, Modelling of the seismic behaviour of wall-to-horizontal diaphragm connections in historical constructions: application to a case study ☆. Eng. Struct. **283**, 115791 (2023). https://doi.org/10.1016/j.engstruct.2023.115791
49. N.R. Devi, S.K. Beura, P.K. Dhir, P. Sarkar, Strain-rate dependence of the mechanical properties of cellular lightweight concrete: experimental study and analytical modeling with multigene genetic programming. Pract. Period. Struct. Des. Constr. (2023). https://doi.org/10.1061/PPSCFX.SCENG-1270
50. I. Kutlu, A. Soyluk, A comparative approach to using photogrammetry in the structural analysis of historical buildings A comparative approach to using photogrammetry in the structural analysis of historical buildings. Ain Shams Eng. J. (2023). https://doi.org/10.1016/j.asej.2023.102298
51. E. Romero-Sánchez, A. Morales-Esteban, R. Bento, J. Navarro-Casas, Numerical modelling for the seismic assessment of complex masonry heritage buildings: the case study of the Giralda tower (Under Review), Springer. Netherlands (2023). https://doi.org/10.1007/s10518-023-01714-x
52. A. Daniela, D.I.R.E. Paolo, P. Achille, Vulnerability assessment of historical masonry buildings to excavation-induced settlements : palazzo assicurazioni generali **26**, 355–360 (2023)
53. I. SAS IP, ANSYS Modeling and Meshing Guide ANSYS, Release 10.0, Technol. Drive Canonsbg. 16 (2005).
54. B. IS: 875 (Part-1) 1987, Code of Practice for Design Loads (Other than Earthquake) for Buildings and Structures, Part-1 Dead Loads - Unit Weights of Building Materials and Stored Materials, 1987.
55. B. IS: 875 (Part-3) 1987, Code of Practice for design loads (Other than Earthquake) for Buildings and Structures Part-3 Wind Loads, in: 2015.
56. A. Kumar, K. Pallav, Structural Identification after Visual Inspection of Brick Masonry Tower using Seismic Assessment, in: 2023: pp. 592–605.
57. A. Kumar, K. Pallav, Finite element analysis of a 108-year-old unreinforced brick masonry tower following the 2015 Nepal earthquakes. Asian J. Civ. Eng. (2023). https://doi.org/10.1007/s42107-023-00902-z
58. A. Kumar, K. Pallav, Old masonary tower analysis visual inspection, NDT, and macro-modeling. Asian J. Civ. Eng. (2023). https://doi.org/10.1007/s42107-023-00766-3
59. L. Binda, A. Saisi, P.S. Test, Application of NDTs to the diagnosis of Historic Structures Résumé Keywords, (2009).
60 A. International, *ASTM C805/C805M-18: Standard Test Method for Rebound Number of Hardened Concrete* (West Conshohocken, PA, 2016). https://doi.org/10.1520/C0805
61. Ş. Sözen, Seismic Performance Assessment and Retro tting Recommendations for a Historic Masonry Building : The Case of Amasya Çilehane Complex, (2024) 0–23.
62. M.L. Leonardi, Evaluation of the seismic behaviour of traditional masonry buildings using an innovative BIM-based approach, (2024). https://doi.org/10.34638/rpee-sIII-n26-004.
63. V. Pérez-Gracia, J.O. Caselles, J. Clapés, G. Martinez, R. Osorio, Non-destructive analysis in cultural heritage buildings: evaluating the Mallorca cathedral supporting structures. NDT E Int. **59**, 40–47 (2013). https://doi.org/10.1016/j.ndteint.2013.04.014
64. I. Standard, Hardened Concrete — Methods of Test, IS 516 (Part 5/Sec 4): Part 5 Non-Destructive Testing of Concrete Section 4 Rebound Hammer Test, 2020.
65. I. Standard, Hardened Concrete — Methods of Test, IS 516 (Part 5/Sec 1): Part 5 Non-destructive Testing of Concrete Section 1 Ultrasonic Pulse Velocity Testing, 2018.
66. R.A. Dameron, V.P. Sbashf, I.P. Lam, Nonlinear seismic analysis of bridge representation and ground motion input ?, 64 (1997) 1251–1269.
67. B. IS: 875 (Part-2) 1987, Code of Practice for Design Loads (Other than Earthquake) for Buildings and Structures, Part-2 Imposed Loads, 1987.
68. I. 1893 (Part-1): Standard, Indian, Criteria for Earthquake Resistant Design of Structures, Part 1 General Provisions and Buildings, 2016.

69. D.M. Boore, Stochastic simulation of high-frequency ground motions based on seismological models of the radiated spectra. Bull. Seismol. Soc. Am. **73**, 1865–1894 (1983)
70. D. Motazedian, G.M. Atkinson, Stochastic finite-fault modeling based on a dynamic corner frequency. Bull. Seismol. Soc. Am. **95**, 995–1010 (2005). https://doi.org/10.1785/0120030207
71. D.M. Boore, SMSIM--Fortran programs for simulating ground motions from earthquakes: Version 2.0.--a revision of OFR 96–80-A, Open-File Rep. (2000) 57. http://pubs.er.usgs.gov/publication/ofr00509.
72. J.R. Kayal, Microearthquake seismology and seismotectonics of South Asia, Microearthquake Seismol. Seism. South Asia. (2008) 1–503. https://doi.org/10.1007/978-1-4020-8180-4.
73. S. Mitra, K. Priestley, A.K. Bhattacharyya, V.K. Gaur, Crustal structure and earthquake focal depths beneath northeastern India and southern Tibet. Geophys. J. Int. **160**, 227–248 (2005). https://doi.org/10.1111/j.1365-246X.2004.02470.x
74. W.K. Mohanty, R. Prakash, G. Suresh, A.K. Shukla, M.Y. Walling, J.P. Srivastava, Estimation of coda wave attenuation for the National Capital Region, Delhi, India using local earthquakes. Pure Appl. Geophys. **166**, 429–449 (2009). https://doi.org/10.1007/s00024-009-0448-7
75 S.K. Singh, M. Ordaz, R.S. Dattatrayam, H.K. Gupta, A spectral analysis of the 21 May 1997, Jabalpur, India, earthquake (Mw = 58) and estimation of ground motion from future earthquakes in the Indian shield region. Bull. Seismol. Soc. Am. **89**, 1620–1630 (1999). https://doi.org/10.1785/bssa0890061620
76. D.L. Wells, K.J. Coppersmith, New empirical relationships among magnitude, rupture length, rupture width, rupture area, and surface displacement. Bull. Seismol. Soc. Am. **84**, 974–1002 (1994)
77. L. Binda, G. Cardani, A. Saisi, C. Groot, A classification of structures and masonries for the adequate choice of repair, Int. RILEM Work. Repair Mortars Hist. Mason. (2005) 20–34. http://www.rilem.net/images/publis/pro067-003.pdf.